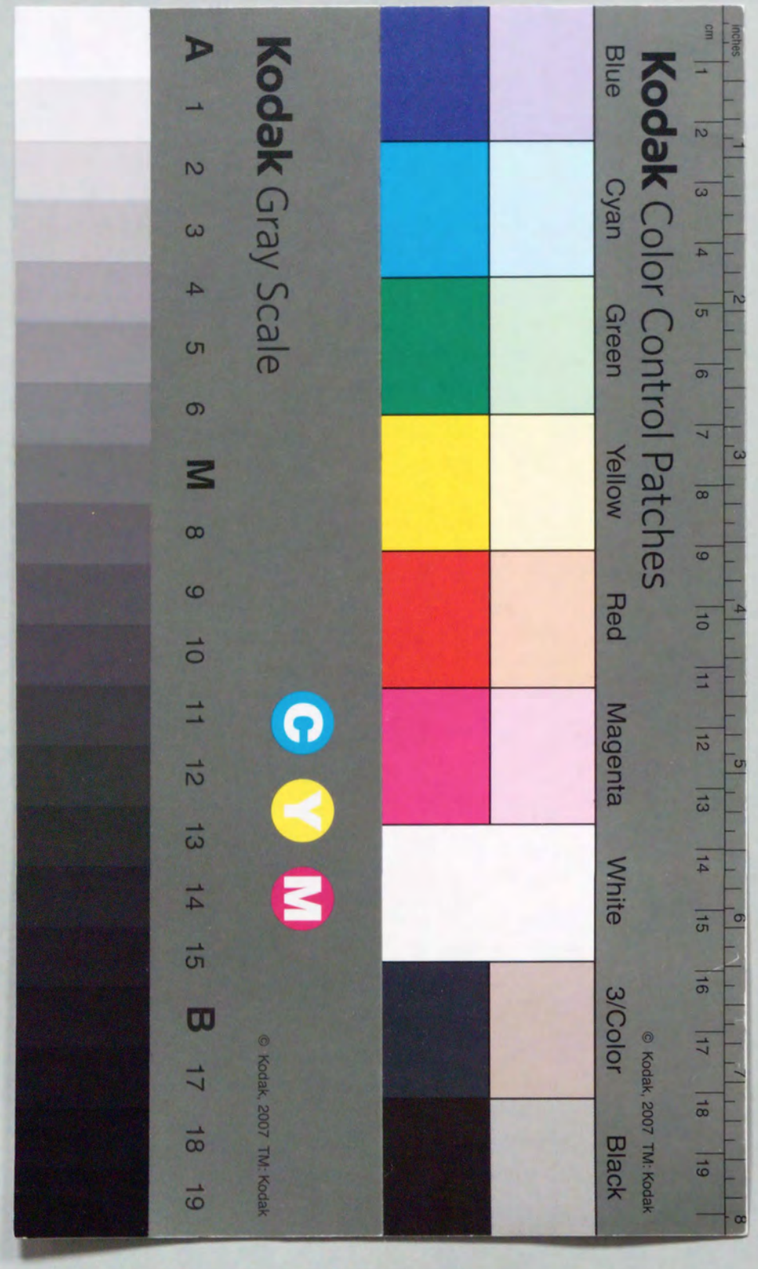

Ballistic electron transport and quantum interference effects in mesoscopic semiconductors

by

Fumiyuki Nihey

DISSERTATION IN PHYSICS

THE OSAKA UNIVERSITY

GRADUATE SCHOOL OF SCIENCE

TOYONAKA, OSAKA

Ballistic electron transport and quantum interference effects in mesoscopic semiconductors

by

Fumiyuki Nihey

Dissertation in Physics

Graduate School of Science
Osaka University

September, 1996

Acknowledgments

The author wishes to express his sincere gratitude to Professor Kazuo Murase, Osaka University, for continuous encouragement and guidance. His suggestions are always valuable. The work could not be accomplished without them. The author is indebted to Professor Sadao Takaoka for valuable discussions and critical reading of the manuscript.

Dr. Kazuo Nakamura, who has led mesoscopic physics in NEC Corporation for many years and gave the author an opportunity for the work, is gratefully acknowledged for daily discussions and encouragement during the work.

The author is grateful to Dr. T. Sakamoto and Dr. S. W. Hwang for their experimental assistance and useful discussions. He is also grateful to Dr. S. Ishizaka for valuable discussions on the calculation of electron transport in mesoscopic structures.

He wishes to thank Dr. A. Okamoto, Dr. H. Toyoshima, and Dr. K. Kasahara for the preparation of high mobility GaAs-AlGaAs heterostructures. He also thanks Dr. S. Matsui, Dr. Y. Ochiai, and Dr. N. Samoto for help in electron beam lithography, as well as Dr. T. Mizuta for providing low-temperature equipment.

He would like to thank Dr. Y. Okuto, Dr. R. Lang, Dr. H. Sakuma, Dr. T. Nozaki, Dr. J. Sone, Dr. T. Itoh, and Dr. M. Kuzuhara for their encouragement during the work.

Special thanks are given to Professor Marc A. Kastner, Massachusetts Institute of Technology, for the collaboration on the last part of the work.

Finally, the author wishes to thank his wife Miho Nihey and their parents for their constant encouragement.

Abstract

Ballistic transport and quantum effects of two-dimensional electron gases (2DEG's) in submicron-sized mesoscopic structures made from GaAs-AlGaAs heterostructures are investigated. Experiments described in this thesis consist of two parts. The first part (Section 4.1) relates the magnetic focusing of ballistic electrons with narrow wires connecting two wide 2DEG reservoirs. The second part (Sections 4.2– 4.5) relates the ballistic transport of 2DEG's in artificially imposed periodic potentials called antidot lattices. The quantization of classical orbits, the interference of backscattered orbits, and the insulator to quantum Hall liquid transition in the structures are discussed. The outlines of these experiments are shown as follows.

Magnetic focusing with parallel wires (Section 4.1)
Magnetoresistance modulation resulting from the magnetic focusing of ballistic electrons is investigated with a pair of wide 2DEG reservoirs separated by etched regions and connected by narrow conducting wires placed in parallel with an equal distance. Distinct peaks in the low field magnetoresistance of the samples are observed when the cyclotron radius and the distance between the wires have commensuration relations. The specularity factor p of electrons for the boundaries of the etched regions is obtained to be $p \approx 1$ from the peak heights. The ballistic length is also derived from the peak heights and found to be much shorter than a mean free path obtained from a Hall measurement. The mechanism limiting the ballistic length is discussed by examining the temperature dependence of the magnetoresistance peaks.

Ballistic transport in antidot lattices (Section 4.2)
Chaotic transport of 2DEG's in antidot lattices, two-dimensional arrays of almost circular depletion regions, is investigated. Typical electron trajectories in the antidot lattices depend strongly on the lattice type and affect low field magnetoresistance. A 2DEG in a triangular lattice of antidots with a large diameter shows a large peak at zero magnetic field whereas a 2DEG in a square lattice of antidots with the same diameter shows small zero-field resistance and a peak at a finite magnetic field.

Quantization of circular orbits in antidot lattices (Section 4.3)
Quantization of classical orbits circulating around a single antidot under magnetic fields is investigated. Due to the quantization, magnetoresistance oscillates with a period of about h/eA as a function of magnetic field, where A is the unit cell area of the antidot lattice. In the magnetoresistance of a 2DEG in a square lattice of antidots, the amplitude of the oscillations has a maximum around a peak where the localized orbits circulating around a single antidot are formed.

Coherent backscattering in antidot lattices (Section 4.4)
Interference of backscattered orbits in antidot lattices is investigated. Due to the interference, the magnetoresistance of a 2DEG in a triangular lattice of antidots shows large amplitude oscillations near zero magnetic field with a period of about $h/2eA$, half of that discussed in the last section. The amplitude of the oscillations has lattice type dependence. For triangular lattices, the amplitude reaches 20% of the zero-field resistance, two order of magnitude larger than those of previous experiments on metal structures. On the other hand, for square lattices, the oscillations are almost invisible. The experimental results are compared with a theory for diffusive electrons.

Insulator to quantum Hall liquid transition in an antidot lattice (Section 4.5)
Experiments on the insulator to quantum Hall liquid transition in an antidot lattice are described. The transition from insulator to quantum Hall liquid shows a fixed point where the magnetoresistance is independent of temperature. Scaling exponents are also determined. The magnetoresistance and the Hall resistance still oscillate with magnetic field with a period of $h/2eA$ in the insulator and h/eA in the quantum Hall state.

Austug

Die ballistische Leitung und der Quanteneffekte der zweidimensionale Electronengases (2DEGs) in untermikrometergroßen mesoskopischen Strukturen aus GaAs-AlGaAs Heterostrukturen werden erforscht. Experimente beschriebt in dieser These besteht aus zweien Teile. Der erste Teil (Sektion 4.1) beschreibt dem magnetischen Fokussierung der ballistischen Elektronen in mesoskopischen Strukturen wo etwas enge Drähte verbinden zweien weiten 2DEG Behälter. Der zweite Teil (Sektionen 4.2–4.5) beschreibt die ballistische Leitung der 2DEGs in künstlichem periodischem Potential genannt Gegenpunktgitter (antidot lattices). Die Quantelung der klassischer Bahnen, die Interferenz der Rückwärtstreuung, und der Isolator-quantisierte Hall Flüssigkeit Übergang in den Strukturen werden erörtert. Das Folgende zeigt dem Umriß diese Experimente.

Magnetischer Fokussierung mit parallelen Drähten (Sektion 4.1)
Magnetoresistenz Modulation aus magnetischem Fokussierung den ballistischen Electronen mit zweien weiten 2DEG Behältern getrennt von geätzten Gegenden und gebunden von etwas parallelen gleichwertigen leitenden Drähten wird erforscht. Klare Spitzen in niederfelder Magnetoresistenz wird gesehen wo der Zyklotronradius und der Abstrand zwischen Drähten haven vergleichenden Verhältnisse. Der Spiegelung Faktor p für der Grenzen den geäzt Gegenden wird $p \approx 1$ aus den Höhen der Spitzen erlangt. Die ballistische Länge wird auch aus den Höhen der Spitzen gezieht, und wird kurzer als mittlere freie Wegänge gezieht aus Hall Messung gefunden. Der Mechanismus, der begrenzt der ballistische Länge, wird von der Temperatur Abhängigkeit der Magnetoresistanz Spitzen erörtert.

Ballistische Leitung in Gegenpunktgitter (Sektion 4.2)
Die chaotische Leitung der 2DEGs in Gegenpunktgitter, zweidimensionale Ordnung der etwa kreisfömigen Verarmungsgegenden, wird erforscht. Typischen electronischen Trajektorien in den Gegenpunktgitter hängen stark von den Typ des Gitter ab, und kommen in niederfelder Magnetoresistenz. Ein 2DEG in einem dreieckigen Gitter mit einem großen Durchmesser zeigt einer großen Spitze in dem nullen Mgnetfeld, aber ein 2DEG in einem quadratischen Gitter mit dem gleichen Durchmesser zeigt klein nullfelder Resistenz und einer Spitze in einem endlichen Magetfeld.

Quantelung der kreisförmigen Bahnen in Gegenpunktgitter (Sektion 4.3)
Die Quantelung der klassischen Bahnen in Gegenpunktgitter wird erforscht. Wegen der Quantelung, schwingt die Magnetoresistenz mit ein Periode von etwa h/eA für der Funktion dem Magnetfeld, wo A ist dem Flächenraum der Einheitzelle dem Gegenpunktgitter. In der Magnetoresistenz dem 2DEG in einem quadratischen Gitter der Gegenpunkte, hat der Umfang der Schwingung einen Höchstmaß in einer Spitze wo lokalisierte Bahnen, die laufen eine Gegenpunkt um, wird geformt.

Kohärente Rückwärtsstreuung auf Gegenpunktgitter (Sektion 4.4)
Die Interferenz der rückwärsstreuenden Bahnen in Gegenpunktgitter wird erforscht. Wegen der Interferenz, zeigt die Magnetoresistenz eines 2DEG in einem dreieckigen Gitter des Gegenpunkte Großamplitude Schwingung in nullen Magnetfeld mit ein Periode von etwa $h/2eA$, der halben Periode der Schwingung in der letzten Sektion. Die Amplitude der Schwingung hat Abhängigkeit von Gittertypen. Für dem derieckigen Gitter, reicht die Amplitude zu 20% der ganzen Resistanz, twei Ordnungen der Größe großer als das vorhergehende Experimente von Metallen Strukturen. Für quadratischen Gitter, ist das Schwingung fast unsichtbar. Die experimental Resultate wird mit einer Theologie für diffus electronen vergleicht.

Isolator-quantisierte Hall Flüssigkeit Übergang in einem Gegenpunktgitter (Sektion 4.5)
Experimente über dem Isolator-quantisierte Hall Flüssigkeit Übergang in einem Gegenpunktgitter wird beschreibt. Der Übergang aus Isolator zu quantisierte Hall Flüssigkeit zeigt einem Fixpunkt wo die Magnetoresistenz ist unabhäugig von Temperature. Maßfaktoren werden gestimmt. Die Magnetoresistenz und die Hall Resistenz schwingen mit Magnetfeld mit ein Priode von $h/2eA$ in des Isolator Zustand und h/eA in des quantisierte Hall Flüssigkeit Zustand.

Contents

Chapter 1

Introduction

In a macroscopic system which we can see with our eyes, the motion of an object can be described by classical theories such as Newton mechanics and electromagnetics. In a microscopic system such as an atom and a molecule, the behavior of the particles obeys quantum mechanics. Recently, there are growing interests in the "mesoscopic systems" [1, 2] which have intermediate sizes between those of macroscopic and microscopic systems. Rapid advances in microstructure fabrication [3, 4] and high quality crystal growth techniques [5, 6] have enabled us to explore peculiar properties of the mesoscopic structures.

The mesoscopic size can be scaled by characteristic lengths such as the mean free path l_e (average distance between the elastic scattering), the phase coherence length l_ϕ (distance over which an electron maintains its phase coherence), and the Fermi wavelength λ_F (de Broglie wavelength of an electron with the Fermi energy). Semiconductor is suitable material because the Fermi wavelength and the mean free path are so large that structures smaller than these lengths can be fabricated with recent technology. For a two-dimensional electron gas (2DEG) in a GaAs-AlGaAs heterostructure (explained in Chapter 2) the Fermi wavelength is typically 40 nm and the mean free path reaches 1–100 μm at low temperatures ($\sim$ 1 K) [1].

Experiments on the transport of 2DEG's in mesoscopic structures smaller than the mean free path but larger than the Fermi wavelength have shown that the motion of a ballistic electron in such structures can be described as the motion of a classical particle. The electric response of a sample having a number of leads can be evaluated by the billiard model [7, 8, 9], which gives transmission coefficients between the leads. The Landauer-Büttiker formula [10, 11, 12], relates these transmission coefficients to voltages and currents at the leads when the sample is coherent.

Parts of this thesis deal with 2DEG's in artificially imposed periodic potentials. Although the period of the potential is smaller than the mean free path, the sample has rather a macroscopic size. The transport of the 2DEG in the potentials can not be described by the Landauer-Büttiker formula because it is not plausible anymore that the

whole area of the sample is coherent. This thesis describes the experiments on the transport of the 2DEG which requires a different approach to describe the conductivity. More importantly, this also provides experimental results on chaotic systems. Electron trajectories in two-dimensional periodic potentials are essentially chaotic. The resistivity of the 2DEG in the potentials can measure an aspect of the chaotic dynamics. Furthermore, when the phase coherence length is much larger than the period of the potential, quantum dynamics in a chaotic system can be probed. This thesis also provides experimental studies on the physics of quantum chaos.

The experiments described in this thesis consist of two parts. The first part (Section 4.1) relates the magnetic focusing of ballistic electrons in mesoscopic structures where a couple of wide 2DEG reservoirs are separated by etched regions and connected by a number of narrow wires placed in parallel with an equal distance. From distinct peaks observed in the low field magnetoresistance of the structures, fundamental parameters are obtained such as the specularity factor, which characterizes the scattering at the boundaries of etched regions, and the ballistic length, which measures the linearity of electron trajectories.

The second part (Section 4.2–4.5) relates the ballistic and the quantum transport of 2DEG's in periodic potentials called antidot lattices. The antidot lattice, a two-dimensional array of almost circular depletion regions, can be considered as a Japanese gamble game *pachinko*. The electrons change their trajectories by the antidot potentials as if the pachinko balls take chaotic motions due to the collisions with nails on the pachinko board. The main differences between the antidot lattice and the pachinko board are as follows. (i) The electron motions in antidot lattices are measured by resistivity which relates to the diffusion of the 2DEG. (ii) The chaotic properties of electrons can be controlled by magnetic field. (iii) The antidot lattice become a *quantum pachinko* when the phase coherence length is larger than the period of antidots.

In Section 4.2, chaotic trajectories in the lattice of antidots with a large diameter are examined. The lattice type dependence of magnetoresistance peaks is discussed. In Section 4.3, the quantization of classical orbits circulating around a single antidot under a magnetic field is investigated. Due to the quantization, magnetoresistance oscillates with a period of h/eA as a function of magnetic field. Here, A is the area of the unit cell of the antidot lattice. In Section 4.4, the interference of backscattered orbits in the antidot lattices is discussed. Due to the interference, magnetoresistance around the zero magnetic field oscillates with a period of $h/2eA$, half of that discussed in the last section. The amplitude of the oscillations is very large for 2DEG's in a triangular lattice of antidots. The amplitude is sensitive to the lattice type. In Section 4.5, insulator to quantum Hall liquid transition in a triangular lattice of antidots is described.

Chapter 2

Review of transport properties in mesoscopic structures

2.1 Introduction

Mesoscopic phenomena relating to this thesis are reviewed. As described in the last chapter, transport phenomena in mesoscopic systems can be categorized by the mean free path l_e and the phase coherence length l_ϕ. The Fermi wavelength λ_F characterizes the quantization of electron states. Another interesting scale, having the energy dimension, is a charging energy $e^2/2C$ of a single electron, where the Coulomb blockade may occur [13, 14, 15].

For investigating mesoscopic physics, Si metal-oxide-semiconductor field-effect transistors (MOSFET's) or modulation-doped GaAs-AlGaAs heterostructures are usually used. A GaAs-AlGaAs heterostructure, used in this study, is suitable to study ballistic phenomena because of a large mean free path. We first describe the material. Later, we describe ballistic phenomena and quantum phenomena in mesoscopic structures.

2.2 GaAs-AlGaAs heterostructures

The GaAs-AlGaAs heterostructures are frequently used as starting materials for fabricating mesoscopic structures. The heterostructure is epitaxially grown on a GaAs substrate by molecular beam epitaxy (MBE) or metal organic chemical vapor epitaxy (MOCVD).

A typical GaAs-AlGaAs heterostructure consists of a GaAs buffer layer on top of a semi-insulating GaAs substrate, an undoped $Al_xGa_{1-x}As$ spacer ($x \sim 0.3$), a Si-doped $Al_xGa_{1-x}As$ layer and a Si-doped GaAs cap layer. Figure 2.1 shows the band-bending diagram of a GaAs-AlGaAs heterostructure. Due to the higher electron affinity of GaAs compared to AlGaAs, free electrons activated from the doped AlGaAs layer are transferred to the undoped GaAs buffer layers and form a two-dimensional electron gas (2DEG) at the

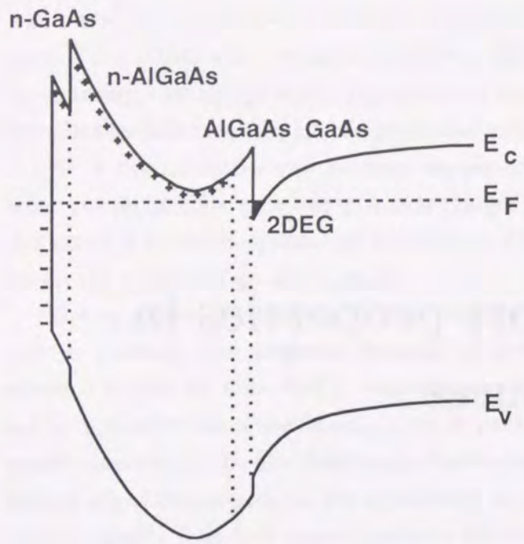

Figure 2.1: Band-bending diagram (showing conduction band minimum E_C, valence band maximum E_V, and Fermi level E_F) of a modulation-doped GaAs-AlGaAs heterostructure. A two-dimensional electron gas is formed in the undoped GaAs buffer at the interface of the AlGaAs spacer layer.

interface of the AlGaAs spacer layer. Because of the strong electrostatic potential at the interface, electron motion perpendicular to the interface are quantized while the electrons can move parallel to the interface. At the surface of the GaAs cap layer, the Fermi level is pinned at almost the middle of the band gap because of high density surface states. The band of the doped AlGaAs layer bends due to the positive charges at donors. Si impurities in AlGaAs make the *DX* center, deep traps involving a large lattice relaxation [16]. Due to the existence of the *DX* centers, the heterostructure shows persistent photoconductvity (PPC) at low temperatures, where photo-excited electrons remain in the conduction band even after turning off the light.

Because the interface between the GaAs layer and the AlGaAs layer can be flat with an atomic scale and with low density of interface traps, boundary scattering at the interface can be negligible. Moreover, since the 2DEG is separated from the doped AlGaAs layer by the AlGaAs spacer layer, the impurity scattering by positively charged donors in the doped layer can be greatly reduced [17]. As a result, electron mobility increases significantly at low temperatures where the electron-phonon scattering is suppressed. Recently reported heterostructures have an electron mobility exceeding 10^7 cm^2/Vs, which corresponds to an electron mean free path of 100 μm [5, 6]. This indicates that the GaAs-AlGaAs heterostructure is suitable for investigating the ballistic transport of 2DEG's.

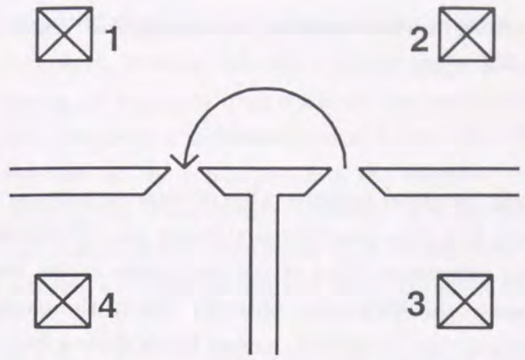

Figure 2.2: Schematic layout of a sample for conventional magnetic focusing experiments. The crossed squares represent Ohmic contacts to the 2DEG. Trajectories leaving the injector point contact (between 2 and 3) around the normal direction are focused onto the collecting point contact (between 1 and 4).

2.3 Ballistic transport in mesoscopic structures

2.3.1 Magnetic focusing of ballistic electrons

One of the interesting phenomena caused by the ballistic motion of 2DEG's in the GaAs-AlGaAs heterostructures is the traverse magnetic focusing of electrons. Electrons emitted from a constriction are focused by magnetic field and enter the other constriction. This technique have been proposed by Sharvin [18] and have used to investigate Fermi spheres and surface condition of films. [19, 20, 21].

van Houten *et al.* firstly investigated the magnetic focusing of a 2DEG in GaAs-AlGaAs heterostructures [22, 23], demonstrating the ballistic motion of the 2DEG. A sample for magnetic focusing experiments is shown in Fig. 2.2. Three wide 2DEG regions are separated by split gates that deplete the 2DEG beneath those gates. Current contacts, 2 and 3, are placed to two reservoirs that are connected through a point contact between a pair of split gates. Voltage difference is measured between another point contact (1 and 4). When the cyclotron diameter of electrons is equal to the distance between the point contacts, the voltage difference between the point contact (1 and 4) increases because electrons emitted from the other point contact enter the collecting point contact and raise the electrostatic potential.

2.3.2 Junction scattering

The ballistic electrons are largely affected by the geometry of the samples. Roukes *et al.* [24] measured the Hall voltage of quantum wires and found that the Hall voltage quenches around $B = 0$; the derivative of the Hall voltage with respect to the magnetic field is almost zero. This is called quenched Hall effect. While many attempts were addressed quantum mechanically, it was appeared that these phenomena are explained by classical mechanics. The origin of the voltage vanishing is boundary scattering at the rounded junction. With the rounding of the corners at the junctions, electrons easily

enter the front channel of the junction even in low magnetic fields because of the wide opening of the wires at the junction [8, 25].

2.3.3 Antidot lattices

There have been many studies on periodic potential systems. One interesting purpose of the studies is making an artificial lattice in a two-dimensional electron gas. Electronic levels make bands because of the Bragg reflections. One of the final goals in the two-dimensional potential systems is to observe the Hofstadter butterfly [26] in the energy spectrum of the system. When the magnetic field is applied, energy levels show a fractal structure which has a period of h/e as a function of magnetic flux threading through one unit of the periodic potential.

When the potential period is smaller than the mean free path of electrons, the transport shows ballistic feature in the conductance of the systems. With an one-dimensional periodic system made by a holographic technique, Weiss *et al* [27] have observed periodic oscillations as a function of the inverse of the magnetic field. When the cyclotron diameter of electrons has a commensurate relation with the period, the drift velocity of the center of the cyclotron motion is largely enhanced [28]. This is also explained by using the broadening of the Landau levels at high magnetic fields [29].

An antidot lattice [30] is one of peculiar potential systems. A two-dimensional periodic potential is so strong that it forms a two-dimensional array of small depletion regions in the 2DEG plane [31]. When the period of the antidots is smaller than the mean free path of electrons, a sequence of peaks appears in the magnetoresistance [32]. The origin of the peaks has been explained with a classical pinball model where the formation of localized orbits enclosing a set of antidots increases the magnetoresistance.

2.4 Quantum effects in mesoscopic structures

2.4.1 Aharonov-Bohm effect

The Aharonov-Bohm effect is predicted by Aharonov and Bohm [33]. Because the vector potential enter directly the phase part of a wave function, the phase of the electron can be changed by the vector potential. This phenomena can be observed in solids. Magnetoresistance oscillations occur with a period of h/e [34] in a normal metal ring because the transmitted waves interfere with each other as shown in Fig. 2.3 (a).

2.4.2 Weak localization

At low temperatures an electron maintains its coherence over a finite distance, even after suffered from multiple impurity scattering. So the phase coherence length can be much

longer than the mean free path. Although the Boltzmann equation [35] ignores the interference between different electron paths which are reflected by multiple impurity scattering, it becomes important at low temperatures that the conductance is altered by the interference of backscattered waves [36]. The coherence of an electron appears as a decrease in the conductance of the samples. Since a magnetic field dephases the interference, the conductance increases as a function of magnetic fields. These phenomena are quantitatively explained with calculations using the Green function expression. A physical explanation is given as the coherent backscattering of electrons [37, 38].

2.4.3 Altshuler-Aronov-Spivak effect

Altshuler, Aronov, and Spivak (AAS) have predicted that magnetoresistance oscillates with a period of $h/2e$ as a function of the flux threading a cylindrical sample. The effect is caused by the interference of the backscattering of an electron as shown in Fig. 2.3 (b). Interference between a pair of backscattered wave survives after the ensemble averaging for the positions of impurities. The amplitude of the conductance oscillations is of the order of e^2/h.

Sharvin and Sharvin firstly observed the $h/2e$ oscillations by using a metal cylinder [39]. The amplitude of the oscillations is very small; 0.1% of the total resistance. The AAS oscillations are observed in various geometries; for example, networks, [40, 41, 42], cylinders, [43, 44, 45, 46], rings [34], and ladders [47].

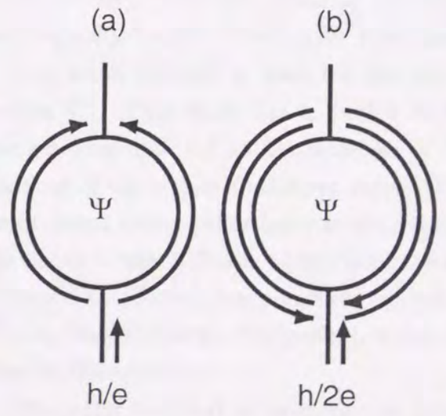

Figure 2.3: Electron trajectories for (a) h/e and (b) $h/2e$ interference effects. Injected electron is shown by arrows at the bottom terminals. Transmitted arrows are shown along the ring.

Chapter 3

Sample preparation and experimental procedure

3.1 Introduction

In this chapter, the procedure of fabricating samples and the setup for measuring the resistance of the samples at low temperatures are described. In the first section, the modulation-doped GaAs-AlGaAs heterostructures used in the study are described. In the second section, the procedures for fabricating the samples including electron-beam lithography process are explained. In the last section, the ^{4}He cryostat, the dilution refrigerator, and the setup of electronics for measuring the low temperature resistance of samples are explained.

3.2 GaAs-AlGaAs heterostructures

Two modulation-doped GaAs-AlGaAs heterostructures, MD806 and MD1341, are used for the studies. They are grown on semi-insulating GaAs (100) substrates by molecular-beam epitaxy (MBE). Their layer structures are shown in Fig. 3.1.

The wafer MD806 is used for the the magnetic focusing experiments described in Section 4.1. This wafer has a graded $Al_xGa_{1-x}As$ layer where the Al fraction linearly changes from $x = 0.3$ at the interface of the doped $Al_{0.3}Ga_{0.7}As$ layer to $x = 0$ at the interface of the doped GaAs cap layer. The two-dimensional electron gas is formed in the undoped GaAs buffer layer at the interface of the undoped $Al_{0.3}Ga_{0.7}As$ spacer layer. The depth of the 2DEG is 62 nm from the surface. The electron density and the mobility measured at different temperatures are listed in Table 3.1. The Fermi wavelength, $\lambda_F = \sqrt{2\pi/n_s}$, and the mean free path, $l_e = \hbar\mu\sqrt{2\pi n_s}/e$, calculated from these values are also listed in the table.

The wafer MD1341 is used for the experiments on the antidot lattices described in

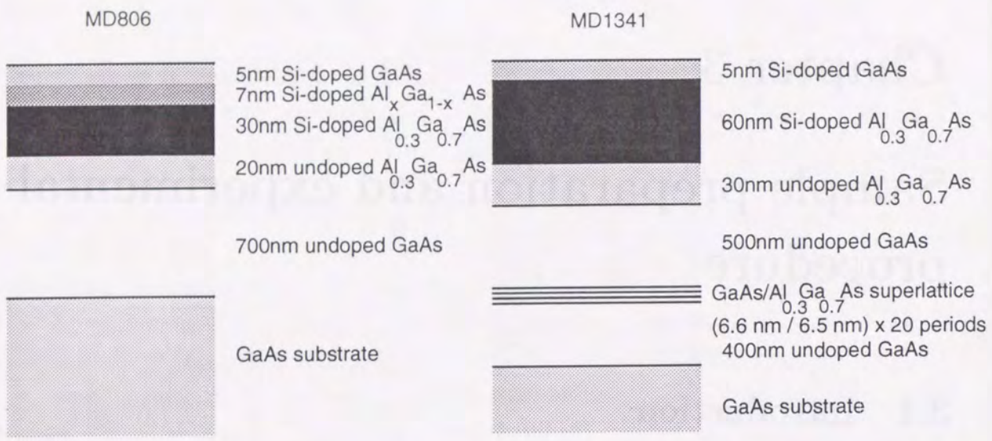

Figure 3.1: Left: the modulation-doped GaAs-$Al_{0.3}Ga_{0.7}As$ heterostructure MD806 used for the magnetic focusing experiments described in Section 4.1. Right: the heterostructure MD1341 used for the studies on antidot lattices described in Sections 4.2–4.5.

Table 3.1: The electron density n_s and the mobility μ_H of the 2DEG in the heterostructure MD806 measured at room temperature, 77 K, and 4.2 K. The Fermi wavelength λ_F and the mean free path l_e calculated from these values are also listed.

Temperature	n_s (10^{11} cm^{-2})	μ_H (cm^2/Vs)	λ_F (nm)	l_e (μm)
RT	2.1	7 300	55	0.055
77 K (light)	5.1	180 000	35	2.1
77 K (dark)	1.9	77 000	58	0.55
4.2 K (light)	5.3	850 000	34	10
4.2 K (dark)	2.1	150 000	55	1.1

Table 3.2: The electron density n_s, the mobility μ_H, the Fermi wavelength λ_F, and the mean free path l_e of the heterostructure MD1341 at room temperature, 77 K, and 1.5 K.

Temperature	n_s (10^{11} cm^{-2})	μ_H (cm^2/Vs)	λ_F (nm)	l_e (μm)
RT	5.9	6 400	33	0.081
77 K (light)	4.6	180 000	37	2.0
77 K (dark)	3.2	200 000	44	1.9
1.5 K (light)	3.7	1 900 000	41	19
1.5 K (dark)	2.8	1 600 000	47	14

Sections 4.2–4.5. The two-dimensional electron gas appears 95 nm below the surface. The GaAs-$Al_{0.3}Ga_{0.7}As$ superlattice layers are inserted in the undoped GaAs buffer layers in order to eliminate crystal defects which grow from the GaAs substrate. The electron density n_s, the mobility μ_H, the Fermi wavelength λ_F, and the mean free path l_e are listed in Table 3.2. The wafer MD1341 has a mobility exceeding 10^6 cm^2/Vs. The heterostructures with high mobility are obtained just before the exhaustion of an Al cell in the MBE.

3.3 Fabrication procedures

The sequence of sample fabrication, shown schematically in Fig. 3.2 is as follows.

Mesa etching (1) AZ photoresist is spin-coated to a thickness of approximately 1 μm on the chemically cleaned surface of a heterostructure wafer. The wafer is prebaked. (2) The photoresist is exposed with a mercury lamp through an optical mask. (3) The exposed parts of the resist are removed with AZ developer, followed by a rinse in water. The wafer is postbaked. (4) The surface of the heterostructure is etched with a mixture of H_2SO_4, H_2O_2, and H_2O (1:8:600) to define the conduction regions. (5) The remaining photoresist is removed with methyl ethyl ketone (MEK), then rinsed in ethanol and water.

Ohmic contacts (6) AZ photoresist is spin-coated again. (7) The photoresist is exposed and developed as in the steps (2) and (3) to form the Ohmic contact electrode patterns. (8) Eutectic alloy of AuGe (88%-12%) is evaporated onto the wafer (typically 1700 Å), with subsequent evaporation of a thin Ni layer (500 Å) and a Au layer (50 Å). (9) The AuGe/Ni/Au layers on the photoresist are removed with the resist layer leaving the metal layers on the heterostructure surface (lift-off technique). (10) The AuGe/Ni/Au layers are alloyed in H_2 or N_2 atmosphare at a maximum temperature of 450°C (temperature

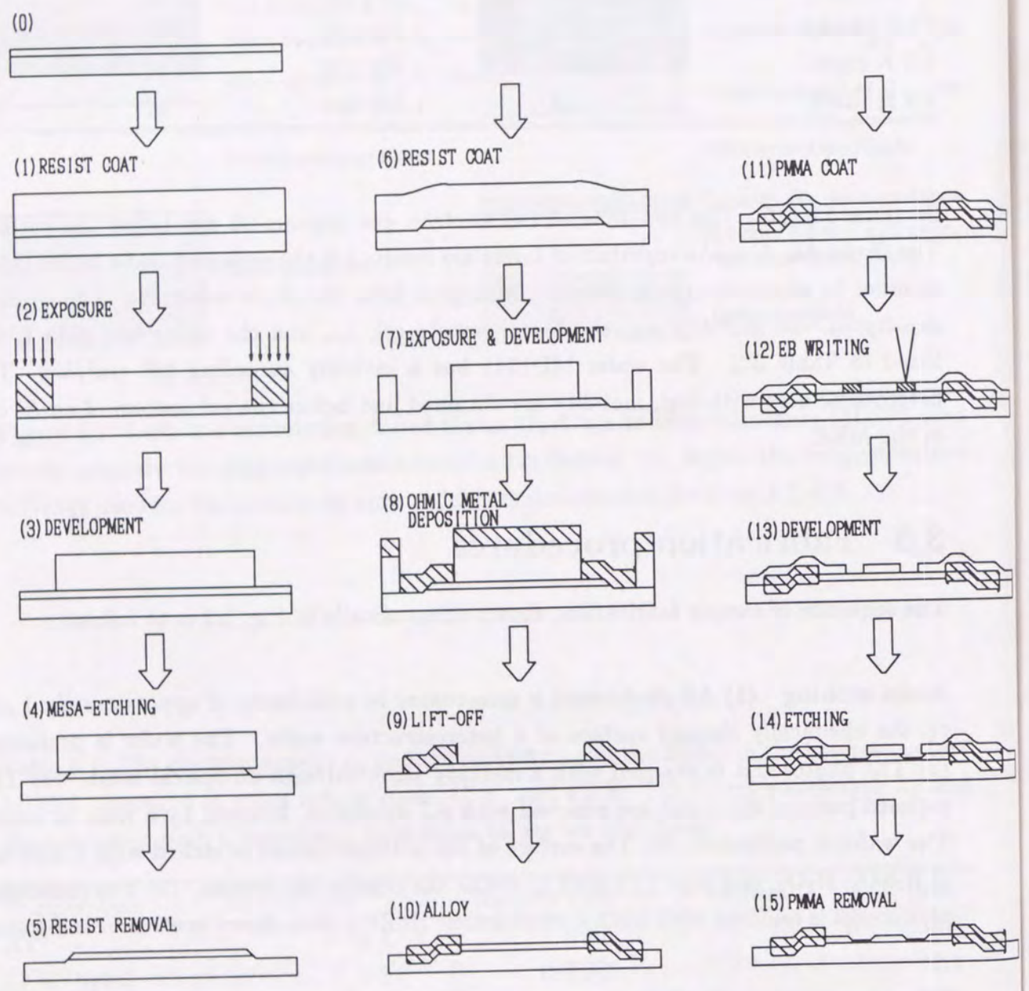

Figure 3.2: Sequence of fabrication procedures for the samples described in the thesis.

increased from 150°C to 450°C for two minutes and then decreased to 150°C for two minutes).

Pads and bonding After electron-beam lithography [procedures (11)-(15)] described in the next sectkon, Au/Ti layers are evaporated onto the Ohmic electrodes for Au wire bonding. Au and Ti layer are also evaporated on the back side of the wafer for soldering to a dual-in package (DIP). The DIP is made from non-magnetic materials. The wafer is scribed and cleaved into chips, which are mounted with a AuSn solder onto a DIP. The electrodes on the chip and the leads of the DIP are connected with Au wires (30 μmϕ) with a thermal bonder.

3.3.1 Electron-beam lithography

For electron-beam lithography, an electron-beam writer JEOL JBX-5FE is used. The maximum acceleration voltage is 50 kV, the minimum beam diameter is 5 nm, and the field size for the maximum resolution is 80 × 80 μm.

The lithography procedure is as follows. (11) Poly(methyl methacrylate) (PMMA) is spin-coated on the surface of a heterostructure to a thickness of approximately 100 nm. This is then prebaked at 160°C for an hour. (12) The PMMA is exposed with the electron beam writer. (13) Next, it is developed in a mixture of methyl isobutyl ketone (MIBK) and isopropyl alcohol (IPA), then rinsed in IPA. (14) The bared surface of the heterostructure is etched with the H_2SO_4:H_2O_2:H_2O mixture. A shallow-etching technique is utilized in which a small amount of the Si-doped AlGaAs layer is slightly left to minimize the lateral depletion at the boundaries of the etched regions. (15) Finally the PMMA is removed by MEK with a subsequent ethanol rinse.

3.4 Electronics for data acquisition

In this section, we describe the helium cryostat [48] and the dilution refrigerator [49] used for resistance measurement. The setup for the measurement is also described.

3.4.1 Helium cryostat

Measurements down to 1.5 K are performed with a liquid-helium cryostat (Oxford Instruments SM-3). The diagram of the cryostat is shown in Fig. 3.3. This has a liquid nitrogen chamber, a liquid helium chamber, and a sample chamber. Each chamber is thermally separated by a vacuum chamber. With a heater mounted to a sample holder in the sample chamber, the temperature of the sample can be changed from 1.5 K to room temperature while operating a 6 tesla superconducting magnet in the helium chamber. Liquid helium can be introduced from the helium chamber to the sample chamber via a

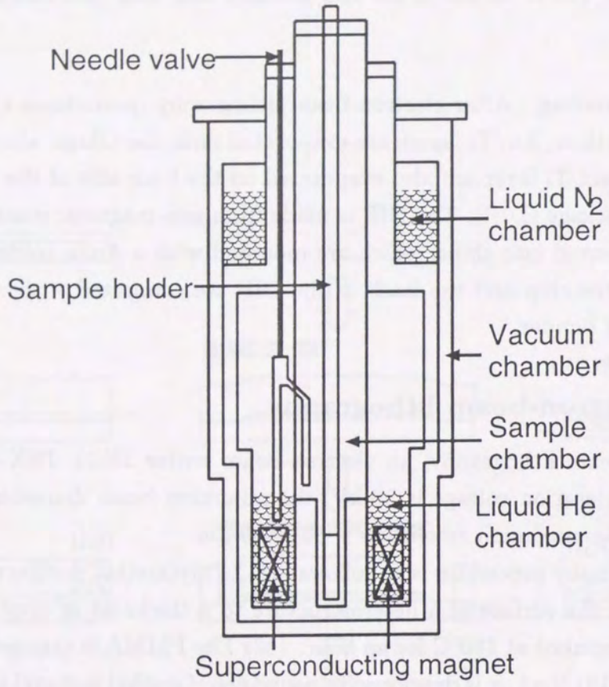

Figure 3.3: A helium cryostat used for measurements above 1.5 K. Liquid helium is transfered from the liquid He chamber to the sample chamber via the needle valve.

needle valve. After closing the needle valve, the sample can be cooled down to 1.5 K by pumping on the sample chamber with a rotary pump.

3.4.2 Dilution refrigerator

A dilution refrigerator (Oxford Instruments Kelvinox 300) is used for measurements below 1.5 K. It has a cooling power of 300 μW at 0.1 K and the lowest temperature of 7 mK. The diagram of the dilution refrigerator is shown in Fig. 3.4.

We describe the essence of the operation principle of the dilution refrigerator. This has a closed circuit filled with the mixture of ^{3}He and ^{4}He gas. At low temperatures, the mixture condenses and separates into two phases in the mixing chamber. One of these phases is almost pure ^{3}He. The other phase is mostly ^{4}He, but even at $T = 0$, it has a 6% ^{3}He impurity. Since the density of the ^{4}He rich phase is larger than that of ^{3}He rich phase, ^{4}He rich phase occupies the lower part of the mixing chamber. If the liquid-vapor interface in the still is kept at about 0.7 K, most of the vapor will be ^{3}He. Pumping on this vapor will remove ^{3}He from the ^{4}He rich phase and destroy the equilibrium between two phases.

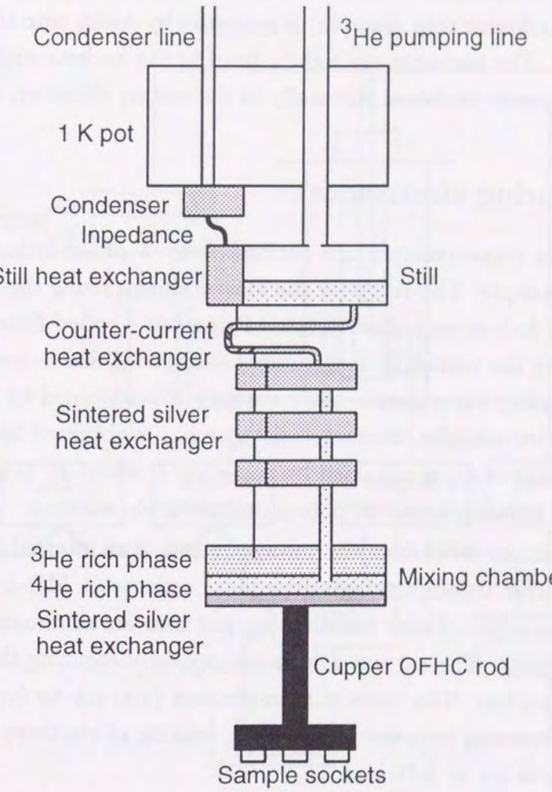

Figure 3.4: Schematic diagram of a dilution refrigerator. In the mixing chamber, ^{3}He rich phase and ^{4}He rich phase are separated. In the still, ^{4}He rich phase and ^{3}He vapor phase are separated.

In order to restore equilibrium, ^{3}He atoms "evaporate" across the phase boundary at the mixing chamber from the ^{3}He rich phase to the ^{4}He rich phase. As the evaporating atoms take heat, the mixing chamber cools down. Due to technological progress in the heat exchange mechanism, such as a silver heat exchanger, we can readily obtain millikelvin temperatures with the dilution refrigerator.

Samples are mounted on three 16-pin sockets for DIP's at the bottom of oxygen free high conductivity copper rod connected to the mixing chamber. In order to make thermal contact, a semiconductor chip (sample) is mounted by AuSn onto the heat sink of an 16-pin DIP package. The packages are tightly fixed to the sockets with screw. Leads to the samples are sufficiently anchored thermally to the mixing chamber, still, and the 1 K pot.

3.4.3 Measuring electronics

Magnetoresistance measurements are performed by a phase-locked alternating current measurement technique. The setup for the measurements using the ^{4}He cryostat is shown in Fig. 3.5. Three lock-in amplifiers (EG&G Princeton Applied Research Model 5210) are used for measuring the current I, longitudinal voltage V_L, and transverse voltage V_T. For the magnetic focusing experiments, the resistance R is obtained by $R = V_L/I$. For measurements on antidot samples, magnetoresistance ρ_{xx} is obtained by $\rho_{xx} = (W/L)(V_L/I)$, and the Hall resistance ρ_{xy} is obtained by $\rho_{xy} = V_T/I$, where W is the channel width and L is the distance between a pair of potentiometric probes.

Alternating current is fed from the voltage output of an internal oscillator (OSC OUT) in a lock-in amplifier through a high-impedance resistor (1 MΩ–1 GΩ) and a reference resistor (1 kΩ) in series. These resistors are put into an aluminum box (Pomona Type 3231) to reduce noise. The current I is monitored by measuring the voltage drop in the 1 kΩ reference resistor. The current is minimized (100 nA to 0.1n nA) corresponding the sample temperatures in order to avoid the heating of electrons [50]. The alternating currnet frequency is set to 8-75 Hz.

The connections to the sample in the cryostat are made with a terminal box made from an aluminum box with 16 BNC female terminals. These terminals connect electrically to 16 pins of the sample socket in the cryostat via twisted wires. The termimal box has switches to short the lines to the ground to avoid electrical shock to the sample.

Data measured by these lock-in amplifiers are transferred to a personal computer (NEC PC-9801ES) via the GPIB (IEEE-488) bus. The computer controls the magnetic field, gets the data, displays them on a screen, and saves them to a hard disk.

The current for the superconducting magnet is provided by a power supply (Oxford Instruments MK3). The output current is controlled by a digital-to-analog converter in an acquisition/control unit (Hewlett Packard 3497A) which is connected to the personal computer via the RS-232C line. The output current is monitored with a digital multimeter

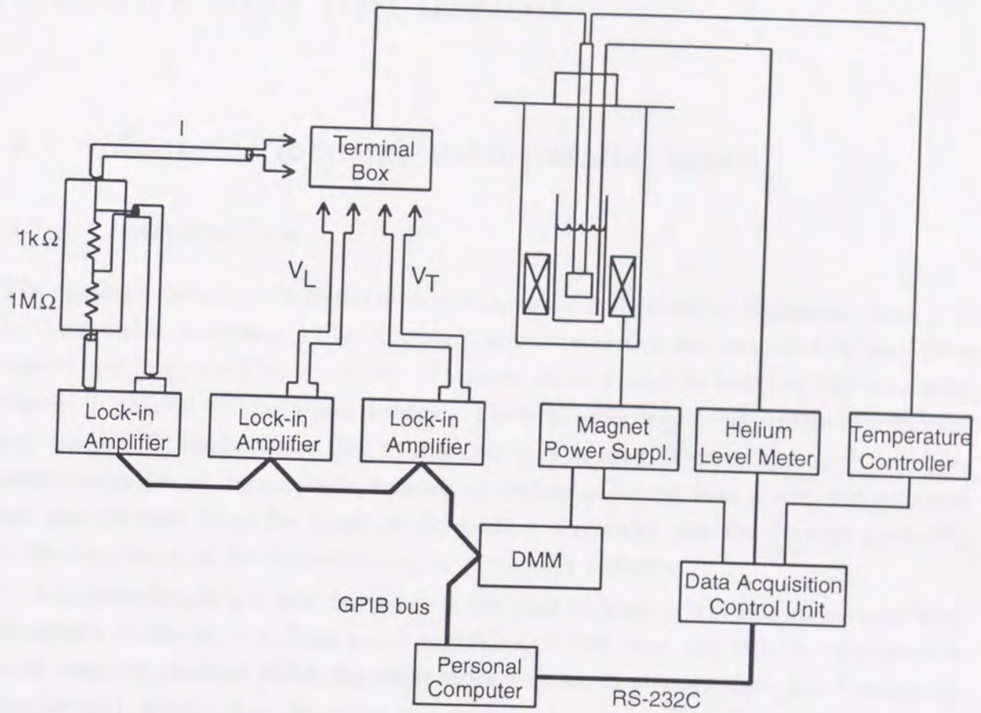

Figure 3.5: The setup of magnetoresistance measurement with ^{4}He cryostat. The lock-in measurements are also utilized for the dilusion refregerator.

(Hewlett-Packard 3457A) by measuring voltage drop at a reference resistance in the power supply. Data are also transferred to the personal computer via GPIB bus.

Chapter 4

Results and discussion

4.1 Magnetic focusing with parallel wires

4.1.1 Introduction

The magnetic focusing of a 2DEG with parallel wires is reported by Nakamura *et al.* [51]. In the samples, as shown in Fig. 4.1, two electron reservoirs are separated by insulating regions and connected by a number of narrow wires placed in between the insulating regions in parallel with an equal distance. The insulating regions are created by focused ion beam (FIB) implantation [52] in that study. The magnetoresistance of the samples shows peaks due to the magnetic focusing of electrons emitted from a wire and collected into another wire. From the height of the peaks it is revealed that the electron scattering at the boundaries of the implanted region is partially diffusive.

A ballistic length l_b is also derived from the peak heights, and found to be larger than the length of the wires l. This result suggests that the wires can still be considered as point contacts, through which the electrons flow adiabatically. Further, l_b is found to be considerably shorter than the mean free path l_e obtained from a Hall measurement on the starting material [51]. The reason for the short l_b is considered to be high sensitivity to small angle scattering, as reported by Spector *et al* [53]. However, it is possible that the samples are degraded by damage which is introduced during the focused ion beam implantation.

In this section, we describe the electron focusing with the same structure but defined by electron beam lithography and wet chemical etching [54]. This can minimize the influence of damage during the fabrication process. Distinct peaks are found in the magnetoresistance of the samples regardless of the wires being longer than l_b. The specularity factor p for the boundaries of the etched regions is obtained to be $p \approx 1$. We find also in this study l_b is much shorter than l_e. To specify the mechanism limiting the short l_b, the temperature dependence of l_b is examined.

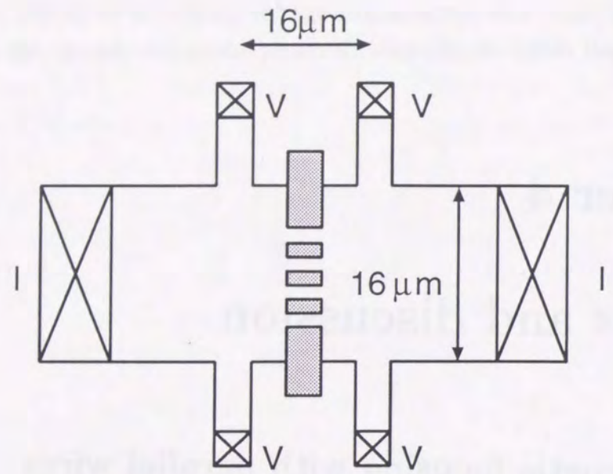

Figure 4.1: Geometry of a sample with wires ($N = 4$) for the magnetic focusing experiments. I's and V's represent current terminals and voltage terminals, respectively.

4.1.2 Experimental procedure

The samples are fabricated from the heterostructure MD806 described in Chapter 3, the same material used in the experiment by Nakamura *et al.* [51] The geometry of a sample is shown in Fig. 4.1, where the shaded regions are defined by electron beam lithography and etched chemically. Narrow wires connect two 2DEG reservoirs in parallel with the separation $s = 2$ μm. Numbers N of the wires are 1, 2, 4, and 6. The length l and the width w of the wires are 4 μm and 0.4 μm, respectively. Voltage drop between the two 2DEG reservoirs is obtained by four-terminal measurements, using lock-in amplifiers operating at 33 Hz and a current of 100 nA with the helium cryostat described in Chapter 3.

4.1.3 Magnetoresistance of parallel wires

Figure 4.2 shows the curves of magnetoresistance R as a function of magnetic field B perpendicular to the 2DEG plane for samples with different numbers of wires at $T = 2$ K under illumination. These curves are normalized by the zero field resistance $R(B = 0)$. At high magnetic fields ($B \gtrsim 0.5$ T), the Shubnikov-de Haas (SdH) oscillations are observed for each sample.

For the sample with $N = 1$, low field magnetoresistance decreases monotonically with increasing magnetic field. This negative magnetoresistance is caused by the depopulation

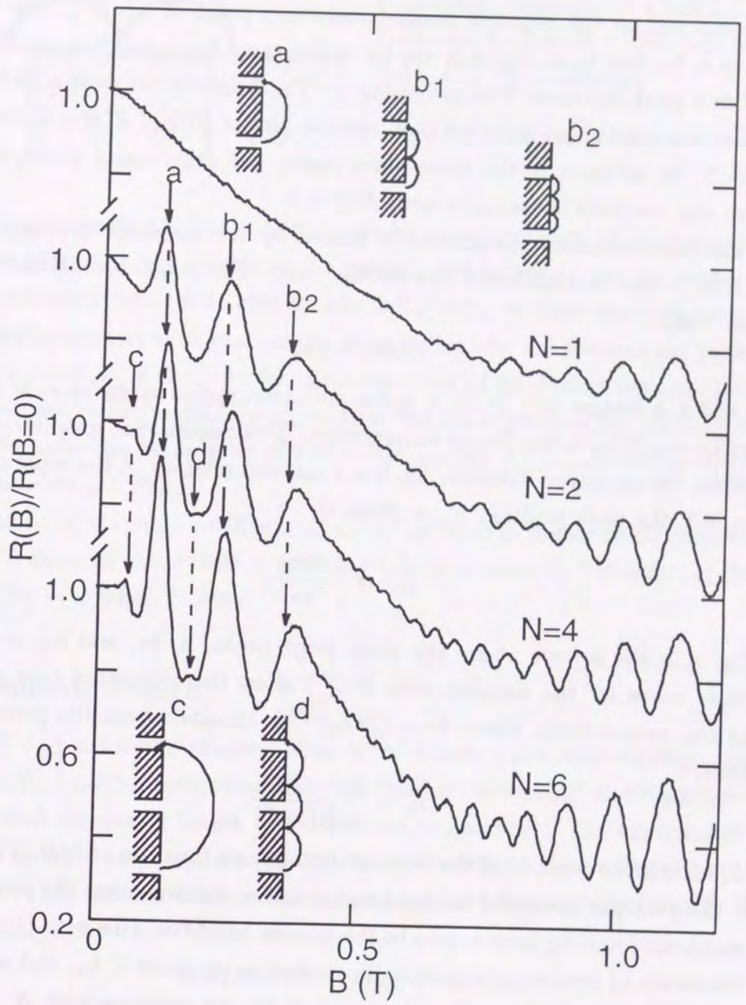

Figure 4.2: Normalized magnetoresistance curves for four samples with different numbers N of wires at $T = 2$ K. Magnetoresistance curves are normalized by zero-field resistance $R(B = 0)$, which are 1016, 462, 233, and 147 Ω for $N = 1$, 2, 4, and 6, respectively. Arrows above peaks indicate the calculated magnetic field position at which the peaks should be observed. Insets show the electron trajectories for each peak.

of quantum channels and the suppression of backscattering within the wires [55, 56]. The negative magnetoresistance is also observed in the samples with $N \geq 2$.

For the samples with $N \geq 2$, in contrast to the sample with $N = 1$, successive peaks are superimposed on the negative magnetoresistance for $B < 0.5$ T. Three large peaks, denoted as a, b_1, and b_2 in Fig. 4.2, appear in the same fields for these samples, and the height of each peak increases with increasing N. The height of the peak a, ΔR_a, measured from a base line connecting adjacent dips, reaches almost 35% of $R(B = 0)$ for the sample with $N = 6$. In addition to the three main peaks, two other small peaks, denoted as c and d, are also resolved for samples with $N \geq 4$.

The magnetoresistance modulation is caused by the magnetic focusing of electrons emitted from a wire and collected into another wire. The magnetoresistance have a local maximum when

$$2ir_c = js, \tag{4.1}$$

where i and j is integer ($i, j \geq 1$), r_c is the cyclotron radius given by $r_c = \hbar k_F/eB$, and $k_F = 2\pi/\lambda_F = \sqrt{2\pi n_s}$ is the Fermi wavenumber. This means that magnetoresistance has a peak when the cyclotron diameter $2r_c$ has a rational relation to the separation of wires. From Eq. 4.1, the peak position B_{ij} is given by

$$B_{ij} = \frac{i}{j}\frac{2\hbar k_F}{es}. \tag{4.2}$$

In Fig. 4.2, the arrows above the three large peaks, a, b_1, and b_2, in each magnetoresistance curve for the samples with $N \geq 2$ show the calculated field positions B_{11}, B_{21}, and B_{31}, respectively, where $k_F = (2\pi n_s)^{1/2}$ is obtained from the period of the SdH oscillations,

$$n_s = \frac{2e}{h}\frac{1}{\Delta(1/B)}, \tag{4.3}$$

where $\Delta(1/B)$ is the periood of the SdH oscilations as a function of $1/B$. The coincidence between the peak positions and the expected positions confirms that the peaks correspond to the magnetic focusing from a wire to the nearest neighbor wire with $(i-1)$ reflections at the boundary of insulating region as illustrated in the inset a, b_1, and b_2 in Fig. 4.2.

The arrows above the small peaks c and d for the samples with $N = 4$ and 6 in Fig. 4.2 indicate the field positions B_{12}, B_{32}, respectively. These peaks correspond to the trajectories entering the second nearest neighbor of an emitting wire as shown in the inset c and d in Fig. 4.2. We find an excellent agreement between the calculated positions and the observed positions.

4.1.4 Specularity factor

The length of trajectory at the peak a is the same as that at the peak b_1 as shown in Fig 4.3. The difference is that at the peak b_1 the electron is reflected at the boundary. So

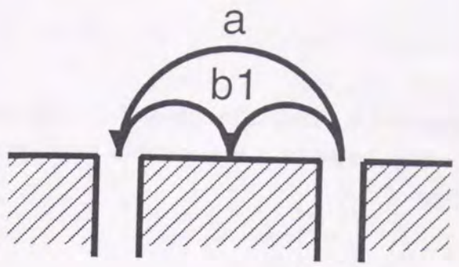

Figure 4.3: Trajectories a and b_1. They have the same trajectory length but b_1 has a reflection at the boundary.

the difference between ΔR_{b1} and ΔR_a measures the specularity of the boundary. In the experiments (Fig. 4.2), the heights of the peaks a and b_1 are almost the same, indicating that the specularity factor p defined by $p = \Delta R_{b1}/\Delta R_a$, is approximately unity.

This result contrasts with that on the wires defined by the focused ion beam implantation, where $p = 0.35$ is obtained for the boundaries of implanted regions [51]. The fact $p \approx 1$ for the wet etched boundary shows that the application of the method to obtain p is reasonable, since the boundaries of wet etched regions are considered to be specular by other experiments [22, 53, 57].

The peak b_2 is relatively small and no peaks are seen in higher fields corresponding to $i > 3$. This is because the cyclotron diameter becomes closer to the width of the wires at high fields ($2r_c = w$ when $B = 0.6$ T).

4.1.5 Ballistic length

The peaks c and d for the samples with $N = 4$ and 6 are considerably smaller than the peaks a, b_1, and b_2, indicating that the number of focused electrons decreases exponentially with increasing length of the electron trajectories. The exponential decrease is confirmed by other experiments [53, 58]. We assume that the observed peak height is proportional to the number of electrons focused into a collecting wire [51, 53]. We define the ballistic length by

$$\Delta R(j) \propto (N - j)\exp(-\pi js/l_b), \tag{4.4}$$

where πjs is the length of the electron trajectory between a pair of wires separated by js. Numbers of possible trajectories between the two wires is $N - j$.

From the ratio of the height of the peak a and that of the peak c (trajectories are shown in Fig. 4.4) for the sample with $N = 4$, we evaluate l_b to be 1.9 μm. This l_b is comparable to the 1.8 μm obtained from the samples defined by the FIB implantation [51]. The ballistic length l_b is five times as small as the mean free path l_e obtained from a Hall measurement on the starting material.

The length of the wires is two times as large as the ballistic length. This suggests that point contacts are not necessarily needed for the magnetic focusing experiments. One

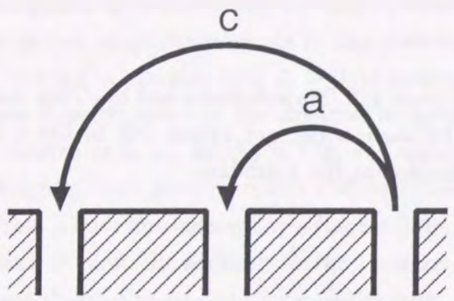

Figure 4.4: Trajectories a and c. The trajectory length of a is two times larger than that of c.

of the reasons why sharp peaks have been observed can be considered that the focusing effect is enhanced by the electron collimation [59] at the exit of chemically etched wires with rounded corners.

4.1.6 Temperature dependence of peak heights

In order to investigate the mechanism limiting l_b, the temperature dependence of the peak height is examined. Figure 4.5 shows magnetoresistance data for the sample with $N = 4$ at temperatures ranging from 2 K to 30 K. Although the amplitude of the SdH oscillations decreases rapidly with increasing temperatures, the heights of low field peaks is unchanged below 8 K. Above 8 K, the peak height gradually decreases, in accordance with the increase in the zero field resistance.

The inset in Fig. 4.5 shows the temperature dependence of l_b and l_e. Similar tendencies of l_b and l_e indicate that the mechanism limiting l_b is the same as that limiting l_e. The fact that no change can be seen below 8 K suggests that the primary mechanism is the ionized remote impurity scattering in this temperature region. For the scattering mechanism in high-mobility GaAs-AlGaAs heterostructure, it has been pointed out that the small angle scattering is a main scattering event [60]. Considering that l_b is sensitive to the small angle scattering, it is reasonable that l_b is much shorter than l_e.

4.1.7 Electron density dependence of peak heights

We examined the electron density dependence of the peak heights. Figure 4.6 shows magnetoresistance data for the sample with $N = 2$ at saturated electron density ($n_s = 5.1 \times 10^{11}\mathrm{cm}^{-2}$) and at half of the value ($n_s = 2.5 \times 10^{11}\mathrm{cm}^{-2}$), controlled by illumination to the sample. For the magnetoresistance with $n_s = 2.5 \times 10^{11}\mathrm{cm}^{-2}$, low field peaks disappear which should exist at the positions indicated by arrows. This suggests the degradation in the ballistic length.

The reduction in peak heights by applying gate voltage over a 2DEG is reported by Spector *et al* [61]. They suggests two possible origins for this effect; decrease in electron

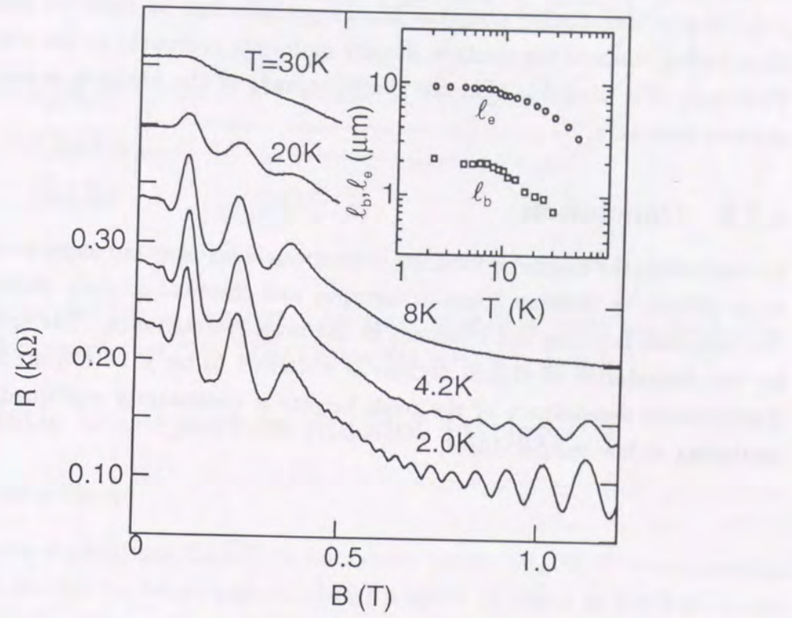

Figure 4.5: Magnetoresistance for the sample with $N = 4$ at different temperatures from 2 K to 30 K. Each curve has been offset upwards from the one below by 50 Ω. Inset shows the temperature dependence of mean free path l_e (circles) evaluated from Hall measurements and ballistic length l_b (squares) obtained from the peak height.

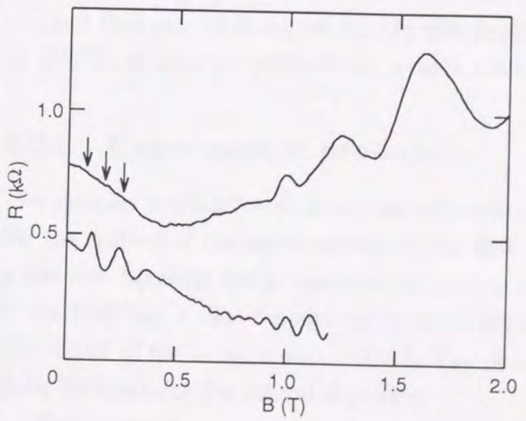

Figure 4.6: Magnetoresistance of the sample with $N = 2$ for different electron density n_s. $n_s = 2.5 \times 10^{11}$ cm^{-2} for the upper curve and 5.1×10^{11} cm^{-2} for the lower curve. The electron density is controlled by illumination to the sample. Arrows on the upper curves indicate the field positions where the peaks should appear.

density and introduction of potential inhomogeneity. For the present case, however, the possibility of introducing potential inhomogeneities can be excluded because the sample illumination controls the electron density uniformly compared to the control with a gate. Therefore, it is plausible that the disappearance of the peaks is caused by decrease in electron density.

4.1.8 Conclusion

In conclusion, the magnetic focusing of electrons is investigated using samples with narrow wires defined by electron beam lithography and chemical etching. Distinct peaks due to the magnetic focusing are observed in the magnetoresistance. The specularity factor p for the boundaries of etched regions is obtained to be $p \approx 1$ from the peak heights. Temperature dependence of the peak heights is consistently explained by the impurity scattering at low temperatures.

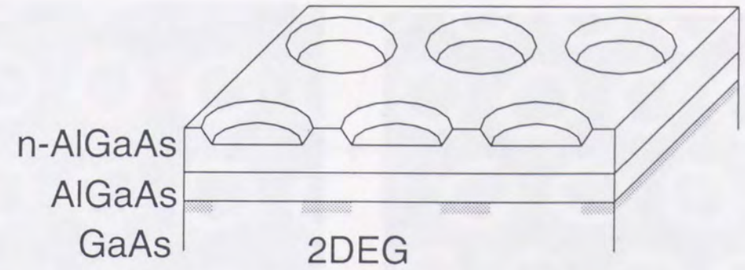

Figure 4.7: An antidot lattice structure. An array of shallow holes are created on a GaAs-AlGaAs heterostructure. The 2DEG below the holes is depleted.

4.2 Ballistic transport in antidot lattices

4.2.1 Introduction

A two-dimensional electron gas (2DEG) in an antidot lattice [31, 30], a two-dimensional array of almost circular depletion regions, shows a series of peaks in low field magnetoresistance [32, 62]. The peaks appear when a commensuration relation between the cyclotron radius and the antidot period is satisfied. Weiss *et al.* [32] attribute the increase in the magnetoresistance to the formation of localized orbits circulating around a set of antidots.

The origin of the peaks is explained by other groups with different ways. Fleischmann *et al.* [63] have analyzed chaotic trajectories in smooth antidot potentials and obtained conductivity with the Kubo formula [64]. They attribute the increase in the magnetoresistance to the quasi-periodic orbits circulating around an antidot. Baskin *et al.* [65] have shown that "runaway" trajectories, traversing along a array of antidots, increases σ_{xx} and thus ρ_{xx} when $\sigma_{xx} \ll \sigma_{xy}$. In this section, experiments on the magnetoresistance of 2DEG's in antidot lattices with a large antidot diameter are described.

4.2.2 Experimental procedure

The samples are fabricated from the heterostructure MD1341 as explained in Chapter 3. On the surface of the heterostructure, the Hall bars with a channel width of 16 μm and a distance between the potentiometric probes of 16 μm are defined. On the whole area of the Hall bar, a two-dimensional array of shallow holes is created as shown in Fig. 4.7. The depth of the holes is about 600 Å. The doped AlGaAs layer are slightly remained in order to minimize the lateral depletion.

Two lattice types, a square lattice and a triangular lattice as shown in Fig. 4.8 are prepared. The period a of both lattices is 200 nm and the diameter d of the etched holes

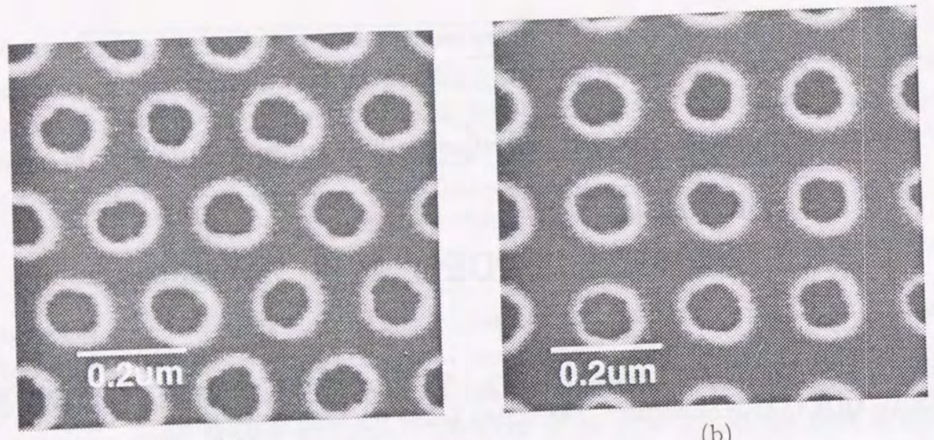

(a) (b)

Figure 4.8: Scanning electron microscope photographs of antidots forming (a) a triangular lattice and (b) a square lattice.

is about 110 nm with a fluctuation of $\sim$ 10 nm. Note that a and d are much shorter than the mean free path in the starting material.

The magnetoresistance ρ_{xx} and the Hall resistance ρ_{xy} of these samples are obtained using a low-frequency lock-in technique (17-75 Hz) with an excitation current of 1-10 nA with the helium cryostat.

4.2.3 Magnetoresistance of antidot lattices

Magnetoresistance curves are shown in Fig. 4.9 (b) for a square and a triangular lattice. These data are obtained at $T = 1.5$ K in the dark. At high fields ($B > 2$ T for the square lattice and $B > 2.5$ T for the triangular lattice) these traces show the quantum Hall profile where each ρ_{xx} drops to zero and ρ_{xy} is quantized to $h/2e^2$ as shown in Fig. 4.9 (a). The electron density n_s is obtained to be 0.9×10^{11} cm^{-2} for the square lattice and 1.3×10^{11} cm^{-2} cm^{-2} for the triangular lattice, assuming that electrons fill the half of the second Landau level at a magnetic field where $\rho_{xy} = h/3e^2$ is satisfied. These values are much smaller than the value 2.8×10^{11} cm^{-2} for the starting material.

The magnetoresistance of the square lattice shows a peak around $B = 0.7$ T, larger than the expected value 0.5 T where the electron circulates around an antidot, i.e., $2r_c = a$ [32]. The deviation is possibly due to the large antidot potential and uncertainty in the electron density. There are no further low-field peaks corresponding to the formation of orbits including more than one antidot (e.g. four antidots) suggesting that antidots have a large diameter enough to avoid such orbits.

The triangular lattice shows magnetoresistance quite different from that of the square

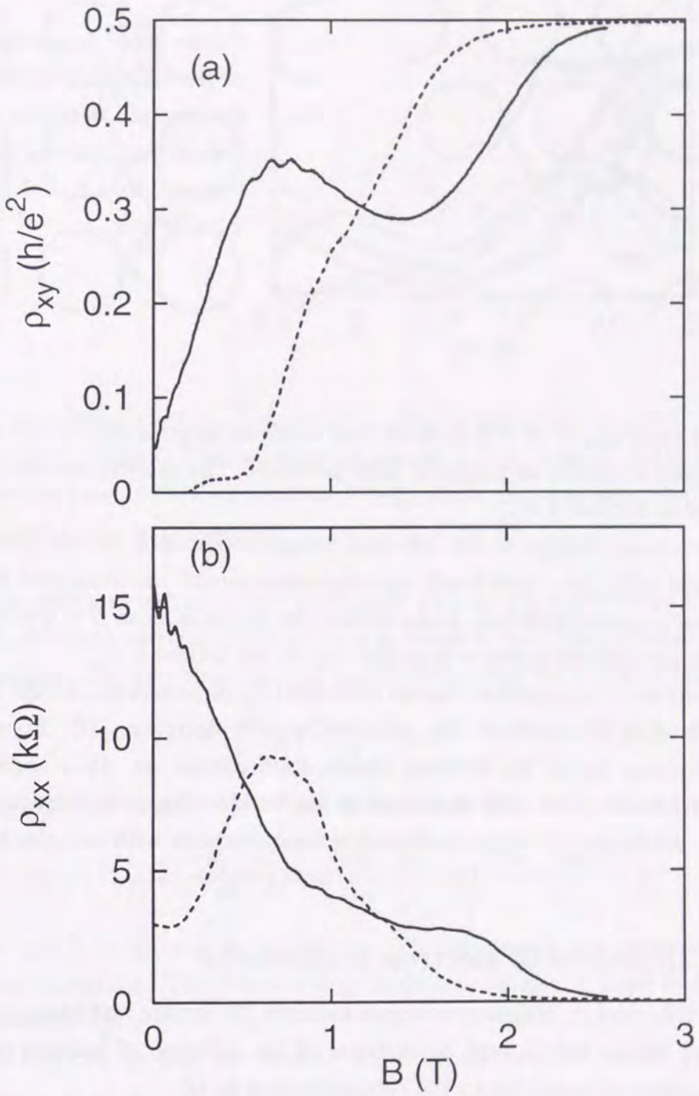

Figure 4.9: (a) The Hall resistance ρ_{xy} and (b) magnetoresistance ρ_{xx} as a function of magnetic field B for a triangular (solid lines) and a square lattice (broken lines) of antidots measured at $T = 1.5$ K in the dark.

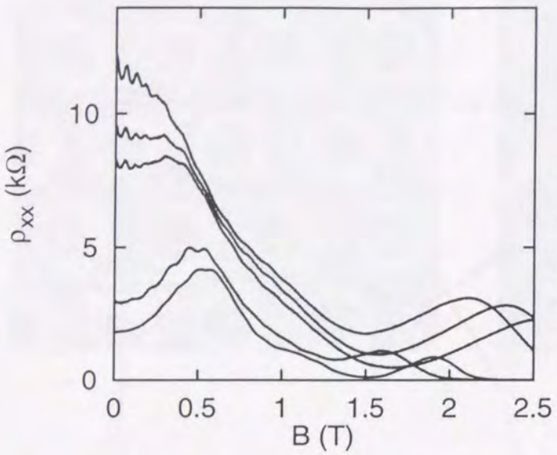

Figure 4.10: Magnetoresistance ρ_{xx} of the triangular lattice with different electron densities n_s. At $B = 0$ the curves, from top to bottom, correspond to 1.6, 1.7, 1.8, 1.9, and 2.3×10^{11} cm^{-2}.

lattice. The value ρ_{xx} at $B = 0$ is about four times as large as that of the square lattice, and drops monotonically as magnetic field increases. The oscillations around $B = 0$ will be discussed in Section 4.4.

The monotonic change in the low-field magnetoresistance for the triangular lattice also contrasts with those previously reported experiments on triangular lattices [66] in which several magnetoresistance peaks appear but no increase at $B = 0$ is observed. This implies that the difference comes from the size of the antidots.

The diameter of the antidots can be controlled by illumination. As the electron density is increased by illumination, the antidot diameter decreases [32]. Figure 4.10 shows magnetoresistance curves for different illumination conditions. It is apparent that the zero field resistance drastically decreases as the antidot diameter decreases. This tendency is also confirmed by magnetoresistance measurements with samples having various diameters.

4.2.4 Calculation of electron trajectories

This great difference in magnetoresistance between the square and triangular lattice can be explained by the lattice type dependence of the diffusion of ballistic electrons. The diffusion constant D is related to the conductivity σ by [1]

$$\sigma = e^2 g D, \tag{4.5}$$

where g is the density of states at Fermi energy. Thus we can evaluate resistivity from the diffusion constant.

When the antidot diameter normalized by the antidot period d/a is much smaller than unity, electrons can go straight over a long distance at $B = 0$. However, when d/a

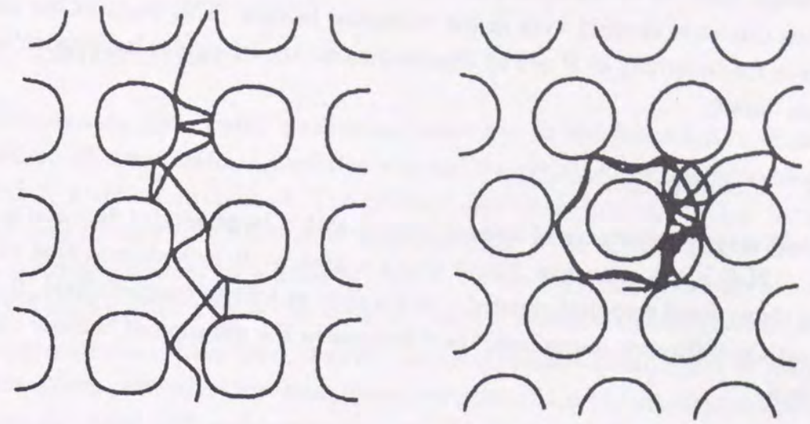

Figure 4.11: Calculated electron trajectories in antidot potentials at $B = 0$. The antidots are indicated by the contour lines where the potential energy is equal to the Fermi energy. Left: a trajectory passing through a square lattice. Right: a trajectory circulating around an antidot in a triangular lattice.

becomes large, electrons can no longer go straight because the motions are blocked by the antidots [67]. We have calculated the electron motions in both lattice types based on the pinball model [63]. We have used smooth antidot potentials for a square lattice,

$$V(\mathbf{r}) = V_0 \left| \cos\left(\frac{\pi \mathbf{a}_1 \cdot \mathbf{r}}{a^2}\right) \cos\left(\frac{\pi \mathbf{a}_2 \cdot \mathbf{r}}{a^2}\right) \right|^2, \tag{4.6}$$

where $\mathbf{a}_1 = (1, 0)a$ and $\mathbf{a}_2 = (0, 1)a$. For a triangular lattice, we have

$$V(\mathbf{r}) = V_0 \left| \cos\left(\frac{\pi \mathbf{a}_1 \cdot \mathbf{r}}{a^2}\right) \cos\left(\frac{\pi \mathbf{a}_2 \cdot \mathbf{r}}{a^2}\right) \cos\left(\frac{\pi (\mathbf{a}_1 - \mathbf{a}_2) \cdot \mathbf{r}}{a^2}\right) \right|^{4/3}, \tag{4.7}$$

where $\mathbf{a}_1 = (\sqrt{3}/2, 1/2)a$ and $\mathbf{a}_2 = (0, 1)a$. The exponents are defined to show the same potential steepness. The Fermi energy is defined to give a diamter similar to the experimental condition.

Figure 4.11 (a) shows that an electron trajectory in a square lattice potential. The antidot diameter is set to half of the antidot period. The trajectory shows an electron tends to move straight in the square lattice potential.

From the calculations with a triangular lattice potential, we obtain a result that contrasts with the square lattice case. Affected by the triangular potential, electrons can not move straight as shown in Fig. 4.11 (b). This implies small diffusion of electrons in the triangular lattice compared to that in the square lattice. As the zero field resistance is inversely proportional to the diffusion constant, the resistivity of the triangular lattice is

much larger than the of the square lattice. When the diameter of antidot becomes small, electrons can move straight even in the triangular lattices. This explains the drastic decreases in the resistivity at $B = 0$ by illumination for the triangular lattice with increasing electron density.

4.2.5 Conclusion

Low field magnetoresistance of antidot lattices with a large antidot diameter is investigated. A 2DEG in a triangular lattice shows a peak at $B = 0$ whereas that of a square lattice shows small zero-field resistivity and a peak at a finite magnetic field. It is suggested that the difference comes from the difference in the diffusion of ballistic electrons at zero field.

4.3 Quantization of circular orbits in antidot lattices

4.3.1 Introduction

The Shubnikov-de Haas (SdH) oscillations occur due to the quantization of the cyclotron orbits. The quantization condition can also be explained by a semiclassical Bohr-Sommerfeld quantization method. The SdH oscillations are periodic in $1/B$ because the enclosed area changes as a function of magnetic field. In an antidot lattice the electron motion is strongly affected by antidot potentials. So the electron can enclose almost same area in different magnetic fields. So the quantization condition can be periodic in B.

Similar oscillations have been observed as the Aharonov-Bohm effect in solids. The Aharonov-Bohm (AB) effect has been commonly observed in the magnetoresistance both of mesoscopic metal [34] and semiconductor [68, 69] rings. Two electron trajectories passing through opposite sides of the ring acquire a relative phase shift proportional to a magnetic flux threading through the ring [33]. According to the phase shift, transmission coefficient of electrons through the ring changes with the period h/e. This effect does not accompany the quantization of the energy states.

Similar effects have been found in systems with quantum dots [70, 71] at high fields. At sufficiently high fields edge states are formed along the boundary of the sample. If the edge state makes a loop along the boundary of the quantum dots they have discrete energy levels because the phase difference acquired after a revolution along the edge state loop should be 2π multiplied by an integer. As the flux through the loop shifts the phase difference, the discrete energy levels successively intersect the Fermi energy and the magnetoresistance oscillates with a period of h/e. Thus the oscillations accompanies the quantization of energy states.

In this section, we describe the observation of the quantization of circular orbits in antidot lattices [72]. The magnetoresistance of 2DEG's in antidot lattices has a peak, as shown in Section 4.2, at a magnetic field where localized orbits encircling one or several antidots are formed [32]. The oscillations observed here are believed to originate from the quantization of the localized orbits around a single antidot.

4.3.2 Experimental procedure

The samples are fabricated from MD1341 heterostructure. The samples have square arrays of antidots with a period of $a = 200$ nm. We prepared samples with three different diameters d of the antidots by changing the exposure time of electron beam. We made measurements at $T \geq 1.5$ K using lock-in amplifiers operating at 75 Hz and a current of 10 nA with the helium cryostat.

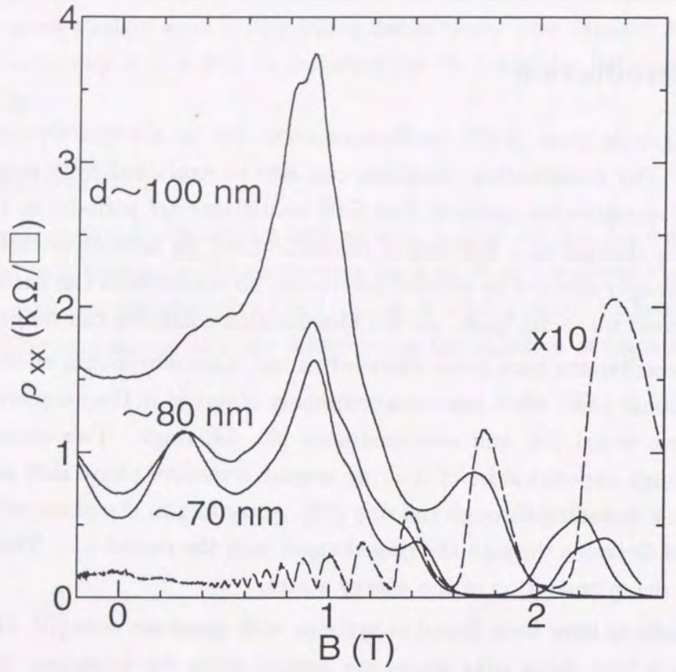

Figure 4.12: Magnetoresistance at $T = 1.5$ K for the antidot lattices with three different diamters d ($d \sim$70, 80, and 100 nm). Magnetoresistance of the starting materials (dashed line)is also plotted.

4.3.3 Magnetoresistance oscillations

Figure 4.12 shows the magnetoresistance ρ_{xx} at $T = 1.5$ K for three antidot samples and for the starting material. At high fields, ρ_{xx} of the starting material shows the Shubnikov-de Haas (SdH) oscillations for $B > 0.4$ T.

We estimate the antidot diameter d from the assumption that $2r_c \sim a - d$ is satisfied at the onset of the quantum Hall regime ($\rho_{xx} \sim 0$). We obtain $d \sim$ 70, 80, and 100 nm for each antidot sample in Fig. 4.12.

For each antidot sample, peaks appear at $B = 0.9$ T which may originate from the formation of localized orbits encircling a single antidot because $2r_c \sim a$ is satisfied at the peak positions [32]. The peaks at $B = 0.3$ T for the samples with $d \sim 70$ and 80 nm are ascribed to the formation of localized orbits encircling four adjacent antidots. For the sample with $d \sim 100$ nm, the peak of this type is not observed, since such localized orbits are blocked by large antidots. These peaks (at $B = 0.3$ T and 0.9 T) are insensitive to temperature because the intrinsic mean free path is much larger than the antidot period

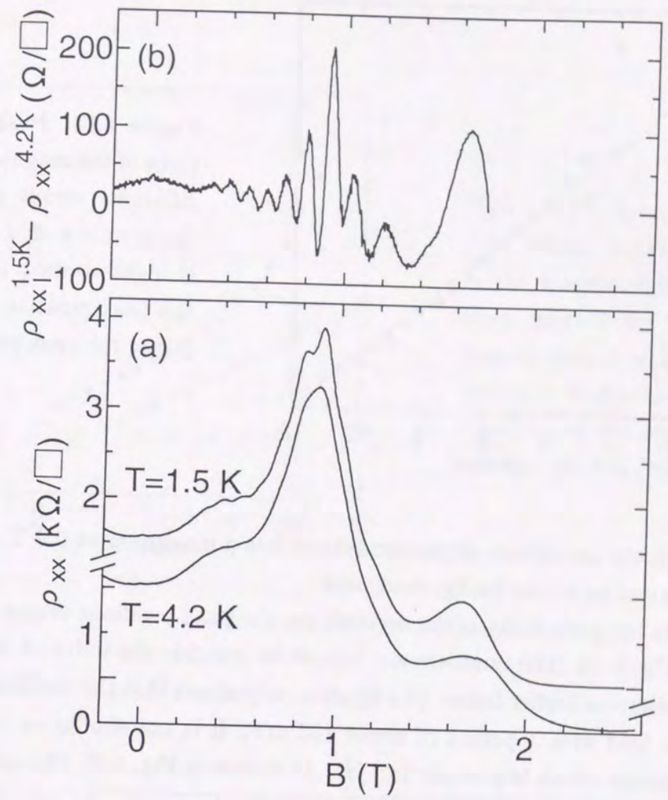

Figure 4.13: (a) Magnetoresistance for the sample with $d \sim 100$ nm measured at $T = 1.5$ K and 4.2 K. (b) Difference between the magnetoresistance curves at $T = 1.5$ K and 4.2 K.

[32].

The most surprising feature for the sample with $d \sim 100$ nm is that fine structures are observed around the peak (0.4 T $\leq B \leq$ 1.0 T) which corresponds to the formation of the localized orbits encircling a single antidot. These structures show different temperature dependence from the background peaks described above.

Figure 4.13 (a) shows the magnetoresistance for the sample with $d \sim 100$ nm obtained at $T = 1.5$ K and 4.2 K. The fine structures are almost invisible in the magnetoresistance at $T = 4.2$ K. In order to extract the temperature dependent part of the magnetoresistance, we subtract data at $T = 4.2$ K from data at $T = 1.5$ K numerically, as shown in Fig. 4.13 (b). This curve shows that the fine structures are likely to oscillate periodically in B rather than in $1/B$ for 0.4 T $\leq B \leq$ 1.0 T although the periodicity breaks for $B > 1$

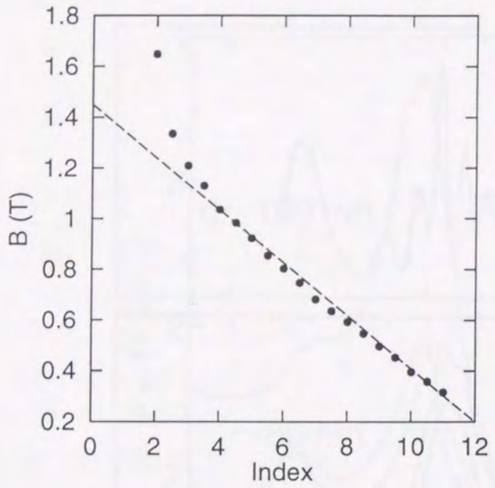

Figure 4.14: Peak (valley) positions of the magnetoresistance oscillations versus peak index for the sample with $d \sim 100$ nm. The straight dashed line is fitted to the peak position for $B < 1.0$ T, giving the peak period of 0.10 T.

T. Moreover, the amplitude of the oscillations has a maximum at 0.9 T, which coincides with the maximum of the background peak.

To clarify the periodicity of the oscillations, the peak positions versus peak indices are plotted in Fig. 4.14. The numbers are defined to coincide the index of the Shubnikov-de Haas oscillations at higher fields. The figure clearly shows that the oscillations are periodic in magnetic field with a period of about 100 mT. It is not similar to the Shubnikov-de Haas oscillations which is periodic in $1/B$. As shown in Fig. 4.15, the oscillations are not periodic in $1/B$.

4.3.4 Antidot diameter dependence

The amplitude of the fine oscillations decreases as the antidot diameter decreases. As shown in Fig. 4.12, the amplitude for the sample with $d \sim 80$ nm is small, and the oscillations disappear for the sample with $d \sim 70$ nm.

Difference between magnetoresistance curves at $T = 1.5$ K and 4.2 K for the sample with $d \sim 80$ nm is shown in Fig. 4.16 together with data for $d \sim 100$ nm. The period of the peak for the sample with $d \sim 80$ nm is obtained as $\Delta B = 96$ mT, which is almost the same as that for the sample with $d \sim 100$ nm. The amplitude of the oscillation for $d \sim 80$ nm is much smaller than that for $d \sim 100$ nm.

4.3.5 Quantization of localized orbits

We estimate that the fine oscillations are believed to be a manifestation of the AB effect. The oscillations are not SdH oscillations because they are periodic in B rather than in $1/B$ as mentioned above. The oscillation period is nearly equal to $h/eA = 103$ mT, where

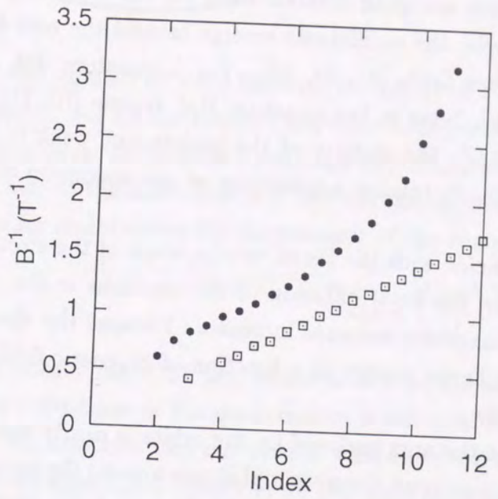

Figure 4.15: Inverse of magnetic field where peaks are observed in the magnetoresistance oscillations plotted for index for the sample with $d \sim 100$ nm (closed circles). Shubnikov de Haas oscillations of the starting material are also plotted (open squares).

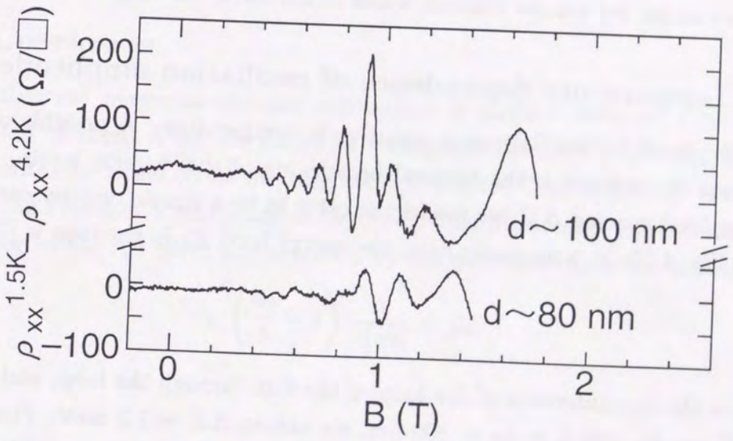

Figure 4.16: Difference between the magnetoresistance curves at $T = 1.5$ K and 4.2 K. Two curves are plotted for the samples with $d \sim 80$ nm and 100 nm.

$A = a^2$ is the area of the unit cell of the antidot lattice, suggesting that the oscillations originate from the quantization of the localized orbits encircling an antidot.

The fields where the oscillations appear are quite different from the fields where usual AB oscillations appear. For a ring sample, the oscillations emerge around the zero field and continue to stay at relatively higher fields [34, 68, 69]. For a quantum dot, the oscillations are observed only in the high fields in the quantum Hall regime [70, 71]. In the present case, the oscillations appear in the vicinity of the background peak (0.4 T $\leq B \leq$ 1.0 T), and the oscillation amplitude reaches a maximum at the maximum of the background peak.

When the discrete energy levels coincide with the Fermi energy, some of the electrons take the localized orbits. Consequently, the total diffusion of the electrons in the antidot structure decreases and thus the magnetoresistance increases. Because the discrete energy levels successively intersect the Fermi energy as a function of magnetic field, the magnetoresistance oscillates periodically.

The oscillation period suggests that the area enclosed by the orbits is nearly equal to A. This can be explained by taking into account the potential slopes around the antidots. Since the repulsive force around the antidots is comparable to the Lorentz force, electrons prefer to move along the bisectors between adjacent antidots and to enclose almost the same area of the order A.

To observe clear AB oscillations, it is necessary that the localized orbits are spatially restricted to enclose a constant area even under different magnetic fields. This is the same requirement as for the narrow channel width of the usual AB ring.

4.3.6 Temperature dependence of oscillation amplitude

The amplitude of the oscillations is sensitive to temperature. A possible origin for the temperature dependence is the thermal broadening of the discrete levels. To calculate the energy level spacing ΔE, we model the orbit to be a simple one-dimensional loop as shown in Fig. 4.17. In a magnetic field, the energy level E_n in the loop is [73]

$$E_n = \frac{h}{2mL^2}\left(n - \frac{e\phi}{h}\right)^2, \tag{4.8}$$

where L is the circumference of the loop, ϕ the flux through the loop, and n an integer. Taking $E_n \sim E_F$ and $L = 4a = 800$ nm, we obtain $\Delta E = 1.3$ meV. The temperature where the thermal broadening becomes dominant, $T = \Delta E/3.5k_B = 4.3$ K, is consistent with the experiments. Note that the half width of the derivative of the Fermi distribution function with respect to the energy is $\sim 3.5k_BT$.

It should be noted that the AB oscillations observed here survive after ensemble-averaging for several hundreds antidots in the samples. The amplitude of conventional AB oscillations in series arrays of metal rings decreases in proportion to the square root

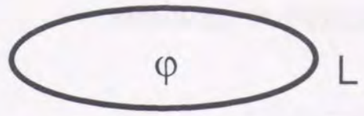

Figure 4.17: A simple loop with a circumference L threaded by a magnetic flux ϕ.

of the number of rings because the phase of the AB oscillations in each ring is sample-specific due to the random impurity configuration [74]. On the other hand, the present samples are made from a relatively impurity-free material and are engraved with the holes of almost the same diameter and the precise periodicity. The allowed deviation of period Δa for maintaining the discreteness of the energy levels is

$$\Delta a < \left(\frac{dE}{dL}\right)^{-1} \frac{\Delta E}{3.5}. \tag{4.9}$$

We obtain $\Delta a < 11$ nm, which is almost the same as the fabrication accuracy, 10 nm. The robustness of the quantization is not clear in the present stage.

We now compare our results with the previous experiments on the AB effect in the antidot structures. Gusev *et al.* [75] have reported oscillations around zero magnetic field ($B < 0.02$ T). They ascribed the oscillations to the coherent backscattering of electrons [76]. Tsubaki *et al.* [77] reports the AB effect in Corbino disks containing square-shaped antidots. Although the amplitude is weak ($< 3\%$ of the total magnetoresistance), the oscillations continue up to 10 T, which suggests that the oscillations originate from a different mechanism from ours.

4.3.7 Conclusion

We have observed magnetoresistance oscillations in antidot lattices. Fine oscillations with a period of about h/eA are found on a magnetoresistance peak resulting from the formation of the localized orbits orbiting a single antidot. The amplitude is temperature dependent, and reaches a maximum at $2r_c \sim a$. This phenomenon is estimated to be a manifestation of the AB effect accompanied by the quantization of the localized orbits.

4.4 Coherent backscattering in antidot lattices

4.4.1 Introduction

In this section, we describe magnetoresistance oscillations in antidot lattices [78] due to the coherent backscattering of ballistic electrons. There are two surprising points. The first is that the amplitude of oscillations is 20% of the zero-field resistivity, two order of magnitude larger than those observed in previous experiments with metallic microstructures. The second is that the amplitude of the oscillations strongly depends on the lattice type. A triangle lattice shows large amplitude oscillations while a square lattice shows invisible oscillations. The sample described in this section are made together with those described in Section 4.2.

4.4.2 Oscillations in triangular lattices

Two sets of low-field magnetoresistance traces for a triangular lattice are shown in Fig. 4.18 (a) and (b) for the temperature ranges 1.5 K $< T <$ 14 K and 0.2 K $< T <$ 1 K, respectively. (The magnetoresistance ρ_{xx} and the Hall resistance ρ_{xy} in wider range of magnetic field is shown in Fig. 4.9.) It is clear from these traces that around $B = 0$ they show oscillations periodic in magnetic field up to 0.3 T. Even though two sets of traces are obtained from two different cool-down procedures, the oscillation periods have the same value of 60 mT in both cases, almost equal to $h/2eA$, where $A = \sqrt{3}a^2/2$ is the unit cell area of the triangular lattice. Furthermore, the maximum of the oscillations always stays at $B = 0$, irrespective of different temperatures and different cool-down procedures.

The amplitude of the oscillations largely depends on temperatures. Figure 4.19 shows the zero-field resistivity $\rho = \rho_{xx}(B = 0)$ as a function of logarithm of temperature. There is a deviation between two sets of data because they have been obtained in different cool-down conditions. Resistivities ρ follows $\log T$, a form for the weak localization in two dimensional systems, although there are deviations at lower temperature range.

The conductivity amplitude $\Delta\rho/\rho^2$ of the oscillations is plotted as a function of temperatures in Fig. 4.20. Here, $\Delta\rho$ is $\rho_{xx}(B = 0)$ minus ρ_{xx} at the first dip. At $T = 0.2$ K, the conductance amplitude reaches $0.27e^2/h$.

The above experimental results suggest that the oscillations have almost the same origin as the $h/2e$ oscillations in the diffusive regime predicted by Altshuler, Aronov, and Spivak (AAS) [76]. The period of the oscillations is determined from half of the magnetic flux quantum for normal metal conductors threading through the mean area of the circular paths, which may be almost the same as the area of the unit cell of the lattices. The temperature dependence is similar to the previous experiments on metals, showing the logarithmic dependence on temperature.

The most peculiar feature in our data is that the oscillation amplitude is very large,

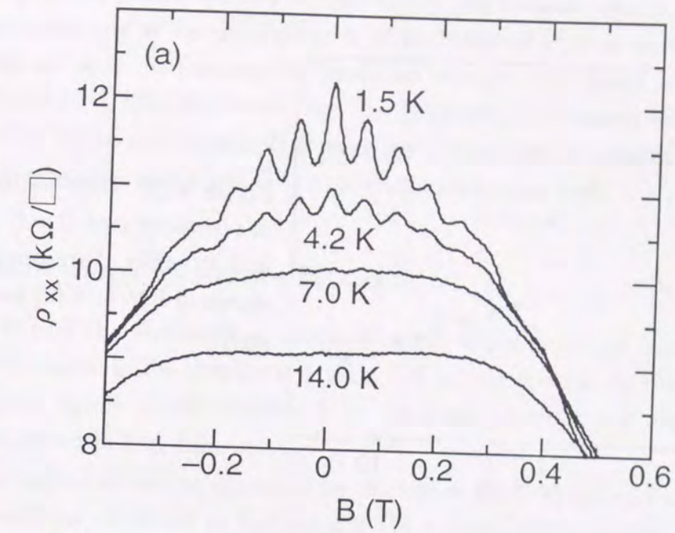

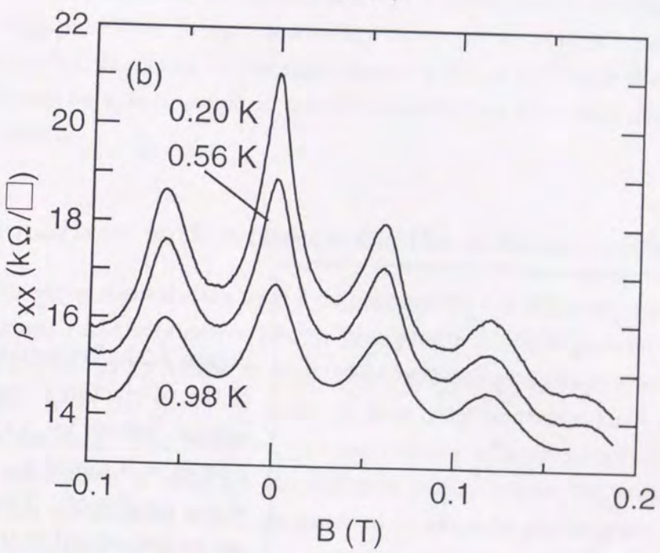

Figure 4.18: (a) Magnetoresistance traces in a triangular lattice of antidots in a temperature range from 1.5 K to 14 K in the dark. (b) Magnetoresistance traces in the range of 0.2 K $\leq T <$ 1 K. The electron density may be a little different from that of (a). Note that no traces in (a) or in (b) are offset.

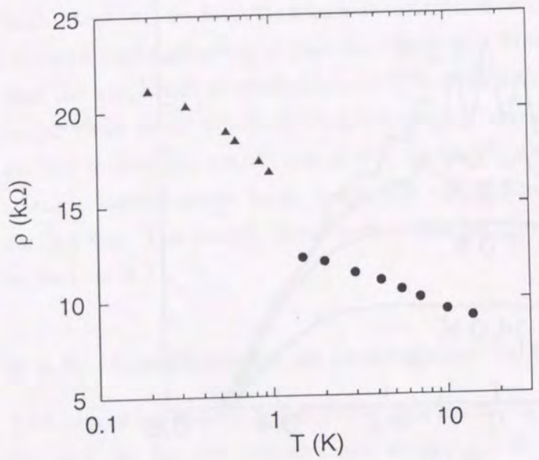

Figure 4.19: Temperature dependence of resistivity ρ at $B = 0$. Closed circles and triangles correspond to the data shown in Fig. 4.18 (a) and (b), respectively.

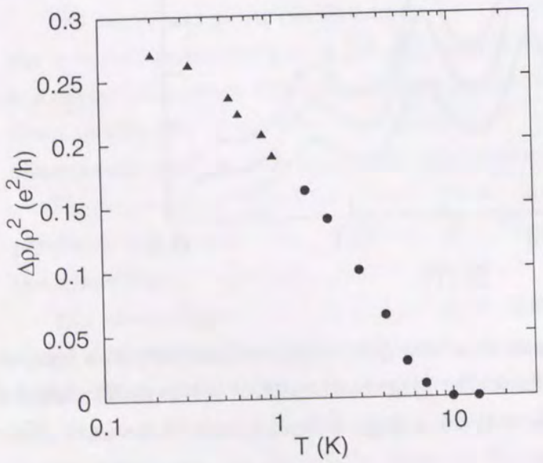

Figure 4.20: Temperature dependence of the conductance amplitude of oscillations, defined by $\Delta\rho/\rho^2$. Here, $\Delta\rho$ is ρ at $B = 0$ minus ρ_{xx} at the first dip of the oscillation. The circles and triangles correspond to the measurements of (a) and (b), respectively.

reaching 20% of the zero-field resistivity as shown in Fig. 4.18, more than two orders of magnitude larger than those observed in metallic structures ($\lesssim 0.1\%$). This can also be understood in the framework of the AAS theory [76] because even in our sample the conductance amplitude of the oscillations is of the order of e^2/h as shown in Fig. 4.20. This is consistent with the theoretically predicted value $\sim e^2/h$ which is independent of the sample material in the diffusive regime. The large amplitude comes from the fact that the conductivity of the antidot sample is much lower than that of metallic samples. From this reason, the relative amplitude of the oscillations becomes large.

4.4.3 Oscillations in square lattices

Noteworthy is that the amplitude of the oscillations depends on the lattice type. The oscillations are visible in the triangular lattice, but almost invisible in the square lattice even though the square lattice antidots have the same period a and almost the same diameter d as shown in Fig. 4.9.

This great difference can be explained by the lattice type dependence of the diffusion of ballistic electrons discussed in Section 4.2. In a triangular potential, electrons can not move straight and have a high provability to return to their starting point with a certain circular orbit, as shown in the right figure in Fig. 4.11. Since the interference of circular orbits may be a main origin of the $h/2e$ oscillations, the calculation supports our experimental results.

4.4.4 Comparison with a theory for the diffusive regime

We compare our experimental data with a calculation for the diffusive regime. Doucot *et al.* [79, 80] derived resistivity correction for honeycomb networks consisting of diffusive wires based on the theory by Altshuler *et al.* [76] Conducting region in a triangular lattice of antidots is similar to the geometry although there may be wide regions surrounded by three neighbor antidots. The detail of the calculations is summarized in Appendix A. Although the calculation is valid for the diffusive regime where the mean free path is much smaller than the channel width, we use it to fit our data ignoring the contradiction. In the fitting procedure we used three parameters; the phase coherence length l_ϕ, the mean free path l_e, and the width of wire w.

From the magnetoresistance at $T = 1.5$ K in Fig. 4.18 (a), we obtain a good fitting to the experimental curve, as shown in Fig. 4.21, with $l_\phi = 610$ nm, $l_e = 330$ nm, and $w = 20$ nm.

The mean free path used in the fitting is much larger than the channel width, which is inconsistent with the assumption of the calculation. This result shows that our $h/2e$ oscillations are in the ballistic regime rather than in the diffusive regime. For precise

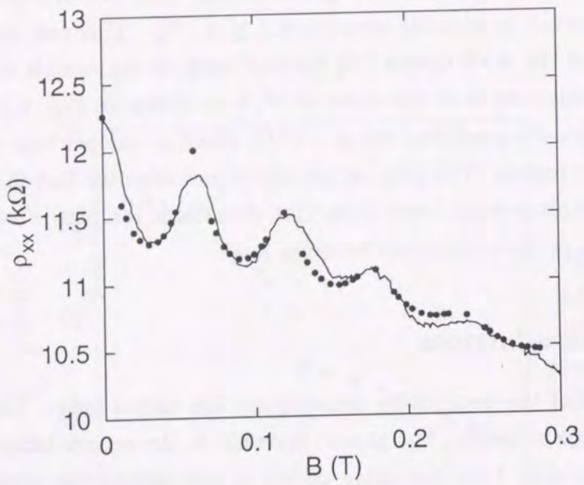

Figure 4.21: Qualitative comparison between the theoretical results (closed circles) and experimental data (solid line) at T = 1.5 K. In this fit, we have l_ϕ = 610 nm, l_e = 330 nm, and w = 20 nm.

comparison with a theory, a calculation for coherent backscattering in the ballistic regime is required.

4.4.5 Conclusion

We have observed large-amplitude $h/2e$ oscillations in antidot lattices. The amplitude of the oscillations reaches 20% of the zero-field resistivities, two orders of magnitude larger than previous results with metallic microstructures. The $h/2e$ oscillations are definitely visible in the magnetoresistance of a triangular lattice but are almost invisible in that of a square lattice. We expect that the probability for electrons to return to their starting points is essential for the lattice type dependence.

4.5 Insulator to quantum Hall liquid transition in an antidot lattice

4.5.1 Introduction

There has been much recent interest in the insulator-to-quantum-Hall-liquid transition (IQHT) in disordered two dimensional electron gas (2DEG) systems in GaAs-AlGaAs heterostructures [81, 82], delta-doped GaAs [83], and silicon metal-oxide-semiconductor field-effect transistors (MOSFET's) [84]. For a 2DEG with longitudinal resistivity $\rho_{xx} \gg h/e^2$ at zero magnetic field, magnetoresistance decreases dramatically with increasing magnetic field. At a critical magnetic field B_c where the magnetoresistance is of the order of h/e^2, the temperature derivative of the resistance changes from negative to positive, so at B_c, the resistivity is independent of temperature. Furthermore, the transition is continuous, showing scaling similar to that seen in the insulator-to-superconductor transition in thin films [85, 86].

In previous experiments [81, 82, 83, 84] the 2DEG has been made insulating by reducing the carrier density. The conductance of the 2DEG decreases more rapidly than linearly with decreasing electron density because the reduced screening enhances scattering from potential fluctuations. In this section we describe experiments on a 2DEG made insulating in a different way; we use a 2DEG in an antidot lattice for the experiment. The disorder in this case presumably arises from the imperfections in the shapes and positions of the antidots. We directly determine the exponent that governs the divergence of the localization lengths on the insulating and quantum Hall sides of the transition, as well as the dynamical exponent that characterizes the IQHT. Although the IQHT is similar to those in disordered 2DEG systems, one feature is surprising. We find that at low magnetic fields the localization length oscillates with magnetic fields with a period of $h/2eA$ and at high magnetic fields the localization length may oscillate with a period of h/eA.

The sample studied in this section is a triangular lattice of antidots fabricated together with the samples described in Sections 4.2 and 4.4. However, the zero-field resistivity is somewhat higher than those previously studied, possibly because of different cool-down procedure. The measurements were carried out in Center for Material Science and Engineering, Massachusetts Institute of Technology. The sample was mounted on the cold finger of a dilution refrigerator with a base temperature of about 25 mK. Both the diagonal resistivity and the Hall resistivity were measured using a lock-in amplifier at 8 Hz with a current of 0.1 nA.

4.5.2 Magnetoresistance at low temperatures

Figure 4.22 shows diagonal resistivities ρ_{xx} versus magnetic field B for different temperatures. The zero-field resistivity reaches 300 kΩ, much larger than h/e^2. By applying B, ρ_{xx}

deceases rapidly. Below the critical field $B_c = 0.47 \pm 0.01$ T, the resistivity decreases with temperatures, whereas above B_c it increases with temperatures. The fixed point occurs where the value of ρ_{xx} is 12.5 ± 0.9 kΩ, close to $h/2e^2 = 12.9$ kΩ. Whereas in conventional disordered 2DEG systems the magnetoresistance decreases monotonically with magnetic field near the IQHT, in the antidot lattice the oscillations are seen at both the lowest and highest fields.

Figure 4.23 shows the diagonal resistivity and the Hall resistivity over a wider range of magnetic field. Very wide Hall plateaus are observed, corresponding to filling factors 2 and 1. At the plateaus, $\rho_{xx} \lesssim 100\ \Omega$. From the transition between these ($B = 4.9$ T), one finds electron density $n = 1.8 \times 10^{11}$ cm^{-2}, lower than the value 2.8×10^{11} cm^{-2} found for the 2DEG without antidots. The onset of the filling factor 2 plateau is very close to B_c, indicating that the transition is from the insulator directly to the quantum Hall liquid.

4.5.3 Localization length in insulator

For a two-dimensional magnetic-field-induced phase transition, the characteristic length scale ξ diverges as $|B - B_c|^{-\nu}$ and the characteristic energy or frequency vanishes as ξ^{-z} [85]. Because the states at the Fermi energy are localized on both sides of the IQHT, we can extract the exponent ν directly from the data.

At $B = 0$, the resistance is typical of a two-dimensional insulator, as illustrated in Fig. 4.24. There $\log \rho_{xx}$ is plotted for $B < B_c$ as a function of $T^{-1/3}$. Below about 1 K, the data follow the Mott variable-range-hopping prediction for two dimensions [87, 88],

$$\rho = \rho_0 \exp\left[\left(\frac{T_0}{T}\right)^{1/3}\right]. \tag{4.10}$$

Fitting the $B = 0$ data for $T < 1$ K to the form $\rho = \rho_0 \exp[(T_0/T)^\alpha]$ we find $\alpha = 0.35 \pm 0.07$. To check the exponent α, we plot ρ_{xx} at $B = 0$ as a function of $T^{-1/3}$ in Fig. 4.25 (a) and as a function of $T^{-1/2}$ in Fig. 4.25 (b). The exponent is 1/2 when electron-electron interaction becomes important [89, 90]. It is clear that below ~ 1 K the resistivity depends linearly on $T^{-1/3}$. We also check the average deviation of the experimental data from a fitting line, $\left(n^{-1} \sum_{i=1}^{n} \{\log \rho_i - \log \rho_0 \exp[(T_0/T_i)^\alpha]\}^2\right)^{1/2}$, where ρ_0 and T_0 are determined to fit the set of resistivities ρ_i at $T = T_i < 1$ K ($1 \le i \le n$) for each α. As shown in Fig. 4.26, the minimum deviation is obtained around $\alpha = 0.35 \sim 1/3$. Thus we can conclude that the resistivity follows Mott's variable range hopping in two dimension with minor electron-electron interaction.

From a fit with $\alpha = 1/3$ we find $T_0 = 5.7 \pm 0.3$ K. The localization length is related to T_0 by [88]

$$\xi = \sqrt{\frac{3}{k_B T_0 g}}, \tag{4.11}$$

where g is the density of states of the two-dimensional disordered system. Because of the antidots, g is less than the density of states $g_0 = m/\pi\hbar^2$ of the unpatterned 2DEG. We

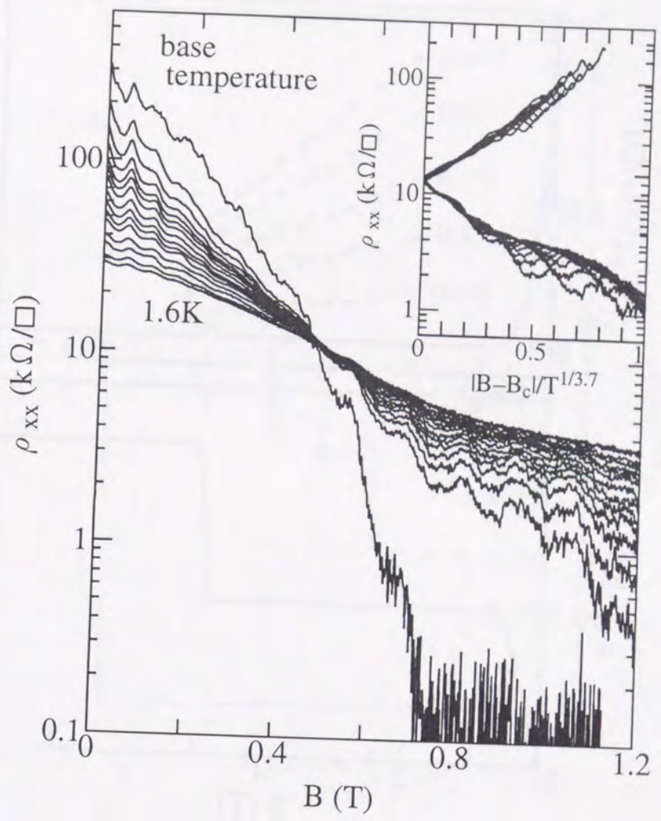

Figure 4.22: Logarithm of diagonal resistivities ρ_{xx} versus magnetic field B. At $B = 0$ the curves, from top to bottom, correspond to temperatures ~0.025, 0.15, 0.20, 0.25, 0.30, 0.35, 0.40, 0.50, 0.60, 0.70, 0.80, 1.0, 1.2, 1.4 and 1.6 K. Data collapse is illustrated in the scaling plot in the inset for $T < 1$ K.

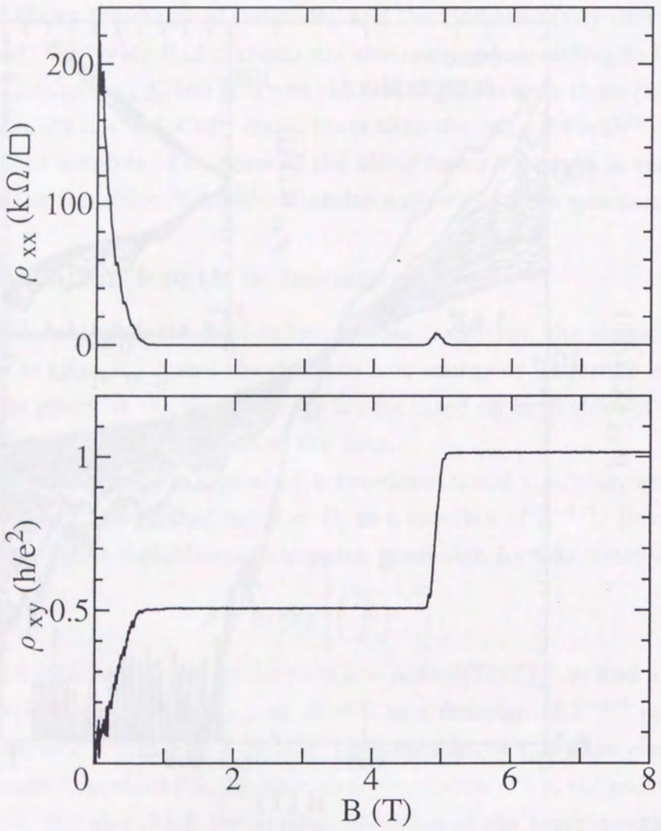

Figure 4.23: Magnetic field dependence of the diagonal resistivity ρ_{xx} and the Hall resistivity ρ_{xy} at the base temperature of the dilution refrigerator $\sim$ 25 mK. The electron temperature may be somewhat higher.

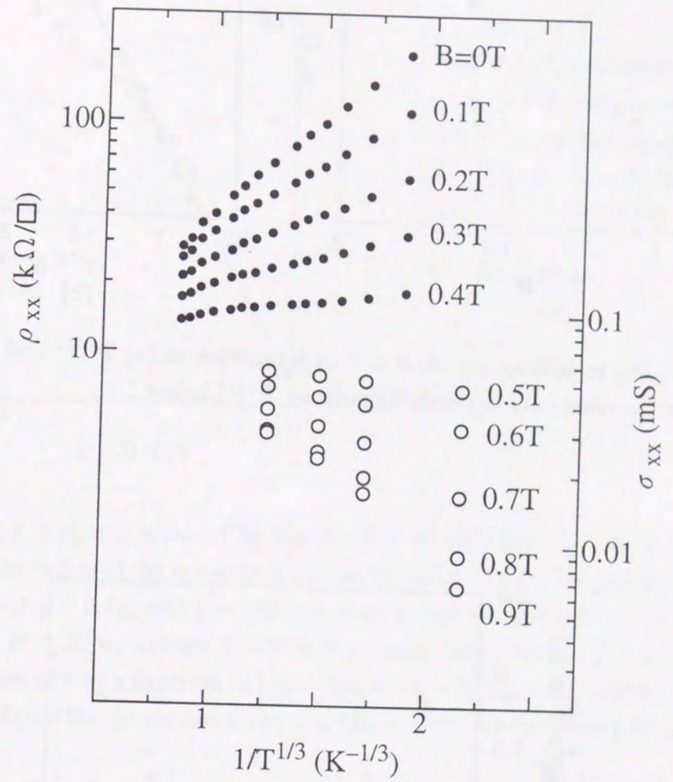

Figure 4.24: Logarithm of the diagonal resistivity ρ_{xx} (closed circles), in the insulator, and the diagonal conductivity σ_{xx} (open circles), in the quantum Hall state, as a function of $T^{-1/3}$ for various magnetic fields. Below $\sim$ 1 K variable range hopping behavior is evident in both quantities.

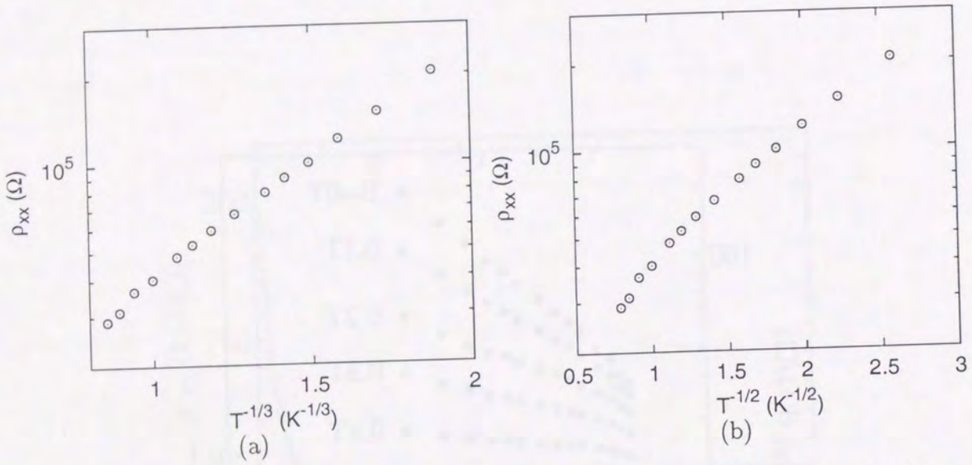

Figure 4.25: The resistivity ρ_{xx} at $B = 0$ as a function of (a) $T^{-1/3}$ and (b) $T^{-1/2}$. It is evident that the resistivity depends linearly on $T^{-1/3}$ below 1 K.

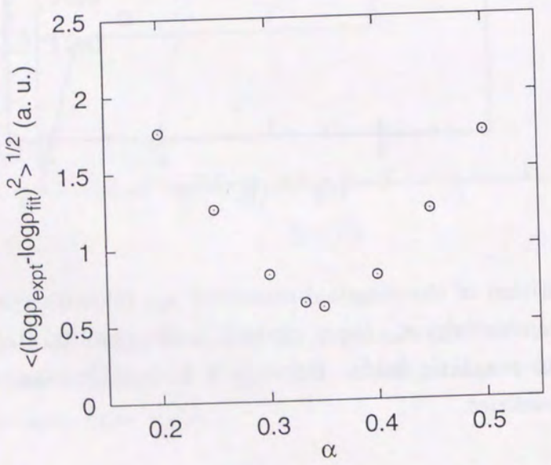

Figure 4.26: Averaged deviation of data from fitting lines. The minimum deviation is obtained around $\alpha = 0.35$.

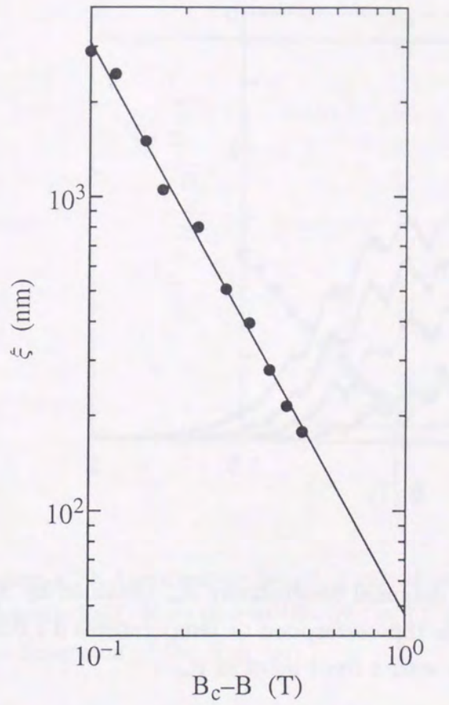

Figure 4.27: Localization length ξ as a function of $B_c - B$, where $B_c = 0.47$ T, plotted for insulating side ($B < B_c$). The slope of the solid line gives an exponent $\nu = 1.86 \pm 0.08$.

estimate that g is simply reduced by the fraction of area depleted by the antidots. We assume that the radius of the antidots is almost the same as the lithographic dimension. In this way we find $g = 0.7g_0$ and $\xi = 180$ nm, close to the antidot lattice constant, 200 nm. For each field $B < B_c$ we extract ξ in this way, using only data for $T < 1$ K. Figure 4.27 shows logarithm of ξ as a function of logarithm of $B_c - B$ where $B_c = 0.47$ T. Fitting the data for $B < B_c$ to the power-law form, $\xi \propto |B_c - B|^{-\nu}$, we find $\nu = 1.86 \pm 0.08$.

4.5.4 Localization in quantum Hall state

Above B_c the dissipation results from hopping between localized states in the quantum Hall liquid. As shown in Fig. 4.28, σ_{xx}, obtained by $\sigma_{xx} = \rho_{xx}/(\rho_{xx}^2 + \rho_{xy}^2)$, decreases as temperature decreases for $B > B_c$, indicating insulating behavior for $B < B_c$ as well as for $B > B_c$. At $B = B_c$ (0.47 T), where ρ_{xx} has a fixed point, σ_{xx} shows a peak, where σ_{xx} has weak temperature dependence, indicating the transition point from insulator to quantum Hall liquid.

For $B > B_c$, as illustrated in Fig. 4.24, σ_{xx} also follows the Mott form

$$\sigma_{xx} = \sigma_0 \exp\left[-\left(\frac{T_0}{T}\right)^{1/3}\right]. \tag{4.12}$$

Therefore, ξ may be extracted by Eq. 4.11 from σ_{xx} in the quantum Hall state, in the

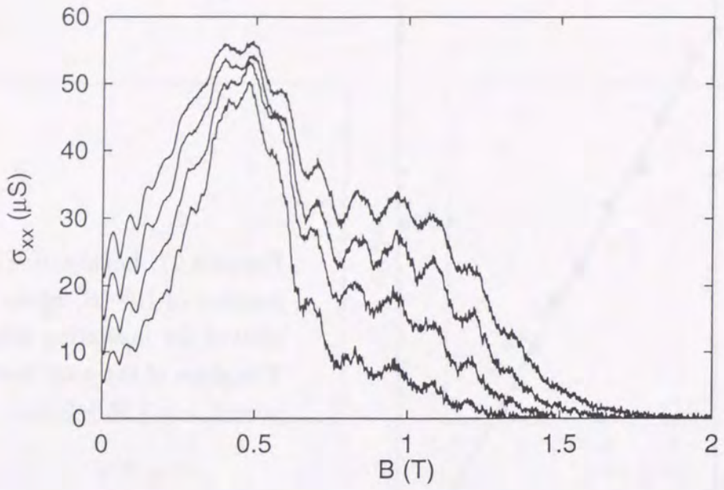

Figure 4.28: Magnetic field dependence of diagonal conductivity σ_{xx} obtained by $\sigma_{xx} = \rho_{xx}/(\rho_{xx}^2 + \rho_{xy}^2)$. The curves from bottom to top correspond to temperatures 0.1,0.2,0.3, and 0.5 K. A peak at $B = 0.47$ T coincides with a fixed point in ρ_{xx}.

same way that we extract it from ρ_{xx} in the insulator. Using this value of ν we plot $\xi^{-1/\nu}$ as a function of magnetic field in Fig. 4.29. This shows that the localization length diverges with the same exponent, $\nu = 1.86$, on both sides of B_c.

4.5.5 Scaling behavior

Studies of disordered 2DEG systems [82, 84] have found good agreement with the proposed scaling relation [85]

$$\rho_{xx} = \rho_0 f_{\pm}(|B_c - B|/T^{1/z\nu}) \tag{4.13}$$

where f_+ is for $B > B_c$ and f_- is for $B < B_c$. To match the variable-range-hopping form we must have the asymptotic behavior $f_-(Y) \sim \exp(Y^{z\nu/3})$ for $Y = |B_c - B|/T^{1/z\nu} \to \infty$. When correlations are important in the insulator one observes the hopping in the Coulomb gap which gives $\rho \sim \rho_0 \exp[(T_0/T)^{1/2}]$ [84, 89, 91] and one would expect the density of states to display critical phenomena. However, for our case we see no evidence of such a gap and conclude that g is weakly dependent on B near B_c. Therefore, as discussed above, $T_0 \propto \xi^{-2} \propto |B_c - B|^{2\nu}$. However, the asymptotic behavior described above requires that $(T_0/T)^{1/3} \propto (|B_c - B|^{z\nu}/T)^{1/3}$, which then requires $z = 2$. Using $\nu = 1.86$ we expect ρ_{xx} to be a function of $|B - B_c|/T^{1/3.7}$, and this describes the data quite well for small $|B - B_c|$, as seen in the inset of Fig. 4.22. It is clear that the oscillations do not scale in this way, because the positions of peaks and valleys are independent of temperature.

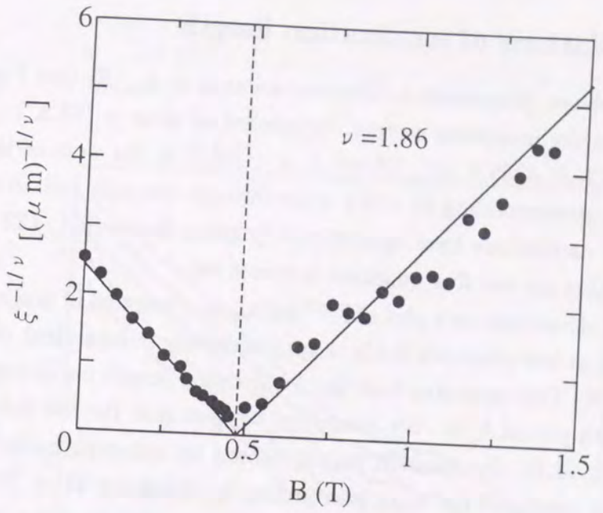

Figure 4.29: Localization length ξ raised to the power $-1/\nu = -1/1.86$ as a function of magnetic field. Note that at $|B - B_c| = 0.1$ T, the localization length is 3 μm, approaching the dimension of the Hall bar.

4.5.6 Comparison with previous studies

The value of ν (1.86) that we find is similar to the value found by Kravchenko *et al.* [84], $\nu = 1.6$, in Si MOSFET's, which show variable range hopping in a Coulomb gap. These authors assume $z = 1$, the value of the dynamical exponent expected for pure Coulomb interactions. Wang *et al.* [82] find that the exponent $\kappa = 1/z\nu = 0.21 \pm 0.02$, in modulation-doped GaAs/AlGaAs heterostructures, consistent with measurements for transitions between adjacent Hall plateaus in the integer quantum Hall effect [92, 93]. Our value of $\kappa = 0.27 \pm 0.02$ is somewhat larger. The samples studied by Wang *et al.* [82] are much closer to the metallic limit at $B = 0$ over the entire temperature range studied by these authors, showing weak localization ($\log T$) resistance rather than the strong localization indicated by variable range hopping resistance. Jiang *et al.* [81] have studied modulation-doped GaAs/AlGaAs heterostructures with higher resistance than those of Wang *et al.* and find variable range hopping with no Coulomb gap as we do. Unfortunately, they have not extracted exponents from their data.

Although the value of $\rho_{xx} = 12.5 \pm 0.9$ kΩ at the fixed point in the antidot lattice is very close to $h/2e^2$, the critical resistance does not appear to be universal. Wang *et al.* [82] report values between 4 and 7 kΩ, Jiang *et al.* [81] found values of ~ 20 kΩ. Hughes *et al.* [83] reports $\rho_{xx} = h/2e^2$, equal to ours, for a delta-doped GaAs.

4.5.7 Oscillations of localization length

As mentioned above, prominent oscillations are seen in $\rho_{xx}(B)$ (see Figs. 4.22 and 4.28). At low fields, in the insulating regime, the period of these is (53 ± 11) mT, close to the value of the $h/2eA = 59.7$ mT, where $A = \sqrt{3}a^2/2$ is the area of the unit cell of the antidot lattice, corresponding to a flux $h/2e$ through the unit cell. At high fields, above the IQHT, the oscillations have approximately twice the period, 122 ± 27 mT, close to 119 mT, the value for one flux quantum per unit cell.

Figure 4.30 shows that on a plot of $T^{1/3} \log \rho_{xx}$ as a function of magnetic field the size of the oscillations at low magnetic fields is approximately independent of temperature from 0.15 K to 0.8 K. This indicates that the localization length oscillates with flux through the antidot with period $h/2e$. We, therefore, suggest that the low field oscillations result from variations of the localization length caused by coherent backscattering. Such an effect has been predicted for weak localization by Altshuler *et al.* [76, 43] and observed by Sharvin and Sharvin [39]. Altshuler *et al.* [76] predict that the $h/2e$ oscillations die out when a flux of order h/e penetrates the conducting annulus surrounding an antidot. The lithographic area of the antidots is about 0.3 of the total, so it is not surprising that only a few periods of the $h/2e$ oscillations are observed.

Figure 4.30 also shows that when $T^{1/3} \log \sigma_{xx}$ is plotted as a function of magnetic field the size of the oscillations at high magnetic field is approximately independent of temperatures. This indicates that these oscillations result from periodic modulation of the localization length in the quantum Hall state. In the high field limit, the localized states in the latter are expected to be those in which an electron is bound to an antidot, so it is not surprising that their radius oscillates with flux through the antidot. Oscillations with period h/eA have also been observed in antidot lattices with higher carrier densities. However, we believe that the latter oscillations have a different origin because the samples are in the ballistic regime, where the mean free path is larger than the lattice constant[78].

Parenthetically, we note that the similarity of the slopes of $T^{1/3} \log \rho_{xx}$ versus magnetic field in Fig. 4.30 is consistent with our previously determined value of $\kappa = 1/z\nu = 0.27$. The scaling function (Eq. 4.13) predicts that the $d \log \rho_{xx}/dB$ at B_c scales as $T^{-\kappa}$. The similarity of slopes in Fig. 4.30 thereby shows that $\kappa \sim 1/3$, close to the value 0.27 determined above.

4.5.8 Conclusion

In conclusion, IQHT in an antidot lattice is investigated at low temperatures. The IQHT is similar to that in other disordered 2DEG systems. There is a fixed point at which magnetoresistance is independent of temperature, and the resistance displays the expected scaling behavior near the fixed point. We have extracted scaling exponent $\nu = 1.86$ that characterize the both sides of the transition. However, the $h/2e$ oscillations of magnetore-

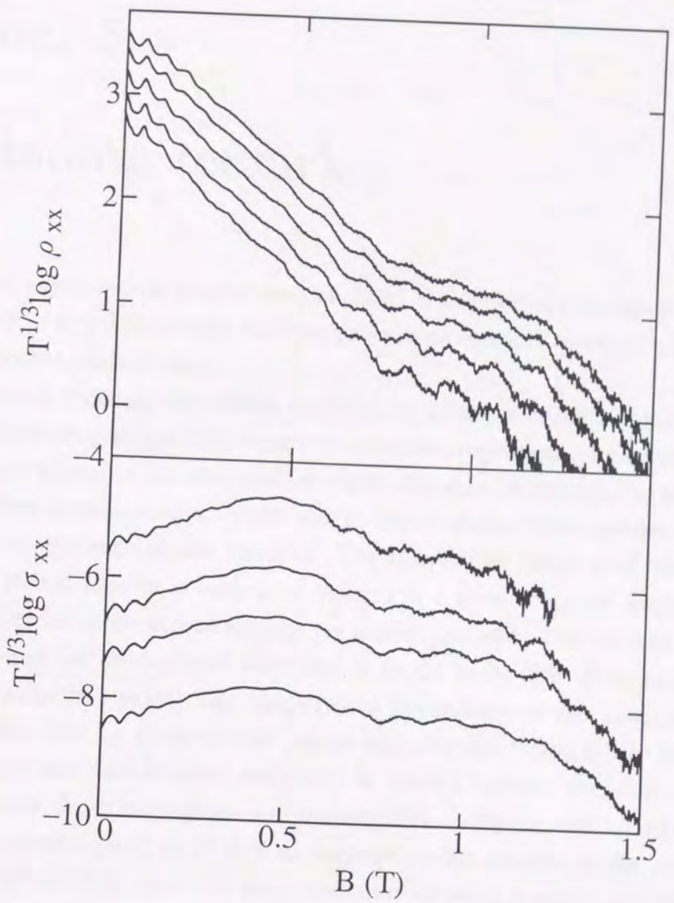

Figure 4.30: Magnetic field dependence of $T^{1/3} \log \rho_{xx}$ (top panel) and $T^{1/3} \log \sigma_{xx}$ (bottom panel). The curves of ρ_{xx} from top to bottom correspond to temperatures 0.15, 0.25, 0.4, 0.6, and 0.8 K, and those of σ_{xx} from top to bottom correspond to 0.1, 0.2, 0.3, and 0.5 K. Because the oscillations in these quantities are approximately independent of temperature, we infer that the oscillations result from periodic variations of the localization lengths.

sistance in the insulator and the h/e oscillations in the quantum Hall state are peculiar to the antidot system. They apparently result from oscillations of the localization lengths.

Chapter 5

Concluding remark

In this thesis, experimental studies are described of the ballistic transport and the interference effects of two-dimensional electron gases in mesoscopic structures fabricated from GaAs-AlGaAs heterostructures.

The magnetic focusing of ballistic electrons is investigated with a pair of wide two-dimensional electron gas reservoirs separated by etched regions and connected by a number of narrow wires placed in parallel with an equal distance. Although the wires are longer than the ballistic length, distinct peaks due to the magnetic focusing have been observed in the magnetoresistance of the samples. The specularity factor p of electrons for the boundary of etched regions is evaluated to be $p \approx 1$ from the peak heights, indicating that the boundaries of the etched regions are almost specular. The ballistic length, measuring the linearity of the ballistic electrons, is found to be five times smaller than the conventional mean free path. The temperature dependence of the peak heights can be consistently explained by the screened remote impurity scattering at low temperatures.

Anomalies in low field magnetoresistance in antidot lattices, two-dimensional arrays of almost circular depletion regions, are investigated. Samples with triangular lattice of large antidots show a peak at $B = 0$ in contrast to the results on the samples with a square lattice of antidots with the same diameter showing a small zero-field resistivity and a peak at a finite magnetic field. Large zero-field resistivity for a triangular lattice is caused by small diffusion of electrons in the potential.

The quantization of localized orbits circulating around a single antidot is investigated. Magnetoresistance of the antidot lattice oscillates due to the quantization with a period of about h/eA, where A is the area of the unit cell of the antidot lattice. The amplitude of the oscillations enhances at a magnetoresistance peak resulting from the formation of localized orbits circulating around a single antidot.

The interference of ballistic electrons in the antidot lattices are investigated. The large-amplitude $h/2eA$ oscillations due to the coherent backscattering are observed around $B = 0$. The amplitude is two orders of magnitude larger than previous experiments on metallic microstructures. The $h/2eA$ oscillations are definitely visible in the resistivity

of the triangular lattice of antidots but are almost invisible in that of the square lattice. We propose an explanation that in the triangular lattices electrons easily return to their starting points and contribute to the interference of backscattered trajectories.

The insulator to quantum Hall liquid transition in an antidot lattice is investigated at low temperatures. The insulator to quantum Hall liquid transition is similar to those in other disordered 2DEG systems. There is a fixed point at which ρ_{xx} is independent of temperature, and the resistance displays expected scaling behavior near the fixed point. We have extracted exponents that characterize the transition for both the insulator and quantum Hall states. The $h/2e$ oscillations of ρ_{xx} in the insulator and the h/e oscillations are observed even in this sample. We find that the oscillations correspond to the oscillations in the localization length.

Appendix A

Coherent backscattering in diffusive honeycomb networks

In this appendix, a formula is shown for quantum correction to the magnetoresistance of diffusive metallic wires forming a honeycomb network [79, 80] as shown in Fig. A.1. The formula is used in Section 4.4.

The correction ΔR by the weak localization [76] to the resistance R of the wire with the length of l, the width w, and the cross section S (the wire is a three dimensional structure), forming a honeycomb network is given by [80]

$$\Delta R/R = \frac{\kappa}{6}\left\{\frac{\eta\cosh\eta-\sinh\eta}{\eta\sinh\eta} - \frac{36}{\pi q}\frac{\sinh\eta\cosh\eta\cdot P'_{p,q}(9\cosh^2\eta-3)}{[A^2-12+8(3-A)^{1/2}]^{1/2}}K\left(\frac{4(3-A)^{1/4}}{[A^2-12+8(3-A)^{1/2}]^{1/2}}\right)\right\}, \quad \text{(A.1)}$$

for $A < 0$, and

$$\Delta R/R =$$

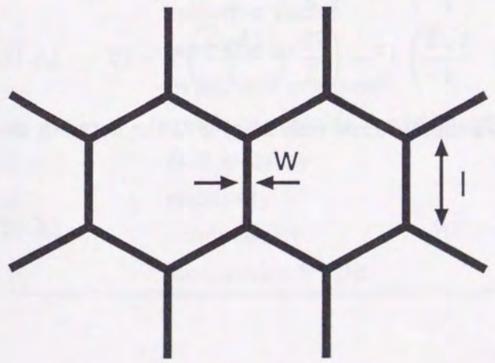

Figure A.1: A honeycomb network geometry consisting of wires with the length of l and the width of w.

$$\frac{\kappa}{6}\left\{\frac{\eta\cosh\eta-\sinh\eta}{\eta\sinh\eta}\right.$$
$$\left.+\frac{18}{\pi q}\frac{\sinh\eta\cosh\eta\cdot P'_{p,q}(9\cosh^2\eta-3)}{(uv)^{1/2}}K\left(\left(\frac{4-(u-v)^2}{4uv}\right)^{1/2}\right)\right\} \quad \text{(A.2)}$$

for $A>0$. Here, $A=P_{p,q}(9\cosh^2\eta-3)$ and for $A>0$, u and v are given by

$$\begin{aligned} u &= \frac{1}{2}(A^2+4A-12)^{1/2} \\ v &= \frac{1}{2}(A^2-4A+4)^{1/2}, \end{aligned} \quad \text{(A.3)}$$

where η is defined by $\eta=l/l_\phi$ and l_ϕ is the phase coherence length. The coefficient κ is defined by $\kappa=2e^2l_\phi/\pi\hbar\sigma_0 S$, where σ_0 is local conductivity of wire before the correction, so $R=l/\sigma_0 S$. The function $K(k)$ denotes the complete elliptic integral of first kind,

$$K(k)=\int_0^{\pi/2}dx(1-k^2\sin^2 x)^{-1/2}. \quad \text{(A.4)}$$

The effect of the width of the wires can be included by replacing the phase coherence length with $l_\phi(B)$ defined by

$$l_\phi(B)=l_\phi(B=0)\left[1+\frac{\pi^2}{3}\left(\frac{2Bwl_\phi}{\phi_0}\right)^2\right]^{-1/2}, \quad \text{(A.5)}$$

where ϕ_0 is quantum flux $\phi_0=h/e$.

The functions $P_{p,q}(\lambda)$ are polynomials of degree q. For $q\leq 5$, they are given by [94]

$$P_{0,1}(\lambda) = -\lambda \quad \text{(A.6)}$$
$$P_{1,2}(\lambda) = \lambda^2-6 \quad \text{(A.7)}$$
$$P_{1,3}(\lambda) = P_{2,3}(\lambda)=-\lambda^3+9\lambda+3 \quad \text{(A.8)}$$
$$P_{1,4}(\lambda) = \lambda^4-12\lambda^2-8\lambda+6 \quad \text{(A.9)}$$
$$P_{1,5}(\lambda) = -\lambda^5+15\lambda^3+\left(\frac{15}{2}+\frac{5\sqrt{5}}{2}\right)\lambda^2-\left(\frac{75}{2}-\frac{15\sqrt{5}}{2}\right)\lambda-15 \quad \text{(A.10)}$$
$$P_{2,5}(\lambda) = -\lambda^5+15\lambda^3+\left(\frac{15}{2}-\frac{5\sqrt{5}}{2}\right)\lambda^2-\left(\frac{75}{2}+\frac{15\sqrt{5}}{2}\right)\lambda-15 \quad \text{(A.11)}$$

The relationship between the nominal two-dimensional resistivity ρ of the network and the resistance R of wires is given by

$$\rho=\sqrt{3}R. \quad \text{(A.12)}$$

List of symbols

Some of the symbols which frequently appear in the text are summarized as follows.

Symbol	Meaning
a	period of antidot lattice
A	area of unit cell of antidot lattice
B	magnetic field
d	diameter of antidot
e	magnitude of electronic charge
E	energy; electric field
E_F	Fermi energy
g	density of states
g_0	density of states in two-dimension ($=m/\pi\hbar^2$, including spin degeneracy)
h	Planck's constant
$\hbar$	Planck's constant ($=h/2\pi$)
I	Current
k_B	Boltzmann's constant
k_F	Fermi wavenumber
l_b	ballistic length
l_e	mean free path
l_ϕ	phase coherence length
n_s	sheet electron density
p	specularity factor
r_c	cyclotron radius
T	temperature
z	dynamical exponent
α	power in variable range hopping function
μ_H	Hall mobility
ρ	resistivity
σ	conductivity
ξ	localization length

Bibliography

[1] C. W. J. Beenakker and H. van Houten, in *Solid State Physics*, edited by H. Ehrenreich and D. Turnbull (Academic Press, San Diego, 1991), Vol. 44, p. 1.

[2] *Mesoscopic Phenmena in Solids*, edited by B. L. Altshuler, P. A. Lee, and R. A. Webb (North-Holland, Amsterdam, 1991).

[3] S. Wolf and R. N. Tauber, *Silicon Processing for the VLSI Era* (Lattice Press, Sunset Beach, 1986).

[4] R. E. Williams, *Gallium Arsenide Processing Techniques* (Artech house Inc., Dedham, 1984).

[5] L. Pfeiffer, K. W. West, H. L. Stormer, and K. W. Baldwin, Appl. Phys. Lett. **55**, 1888 (1989).

[6] T. Saku, Y. Hirayama, and Y. Horikoshi, Jpn. J. Appl. Phys. **30**, 902 (1991).

[7] C. W. J. Beenakker and H. van Houten, Phys. Rev. Lett. **63**, 1857 (1989).

[8] H. U. Baranger and A. D. Stone, Phys. Rev. Lett. **63**, 414 (1989).

[9] H. U. Baranger, D. P. DiVincenzo, R. A. Jalabert, and A. D. Stone, Phys. Rev. B **44**, 10637 (1991).

[10] R. Landauer, IBM J. Res. Dev. **1**, 223 (1957).

[11] R. Landauer, Philos. Mag. **21**, 863 (1970).

[12] M. Büttiker, Phys. Rev. Lett. **57**, 1761 (1986).

[13] J. H. F. Scott-Thomas *et al.*, Phys. Rev. Lett. **62**, 583 (1989).

[14] U. Meirav, M. A. Kastner, and S. J. Wind, Phys. Rev. Lett. **65**, 771 (1990).

[15] H. van Houten, C. W. J. Beenakker, and A. A. M. Staring, in *Single Charge Tunneling*, edited by H. Grabert and M. H. devoret (Plenum Press, New York, 1992), p. 275.

[16] P. M. Mooney, J. Appl. Phys. **67**, R1 (1990).

[17] R. Dingle, H. L. Störmer, A. C. Gossard, and W. Wiegmann, Appl. Phys. Lett. **33**, 665 (1978).

[18] Y. V. Sharvin, Zh. Eksp. Teor. Fiz. **48**, 984 (1965), [Sov. Phys. JETP **21**, 655 (1965)].

[19] V. S. Tsoi, Pis'ma Zh. Eksp. Teor. Fiz. **19**, 114 (1974), [JETP Lett. **19**, 70 (1974)].

[20] V. S. Tsoi, Zh. Eksp. Teor. Fiz. **68**, 1849 (1975), [Sov. Phys. JETP **41**, 927 (1975)].

[21] V. S. Tsoi and I. I. Razgonov, Zh. Eksp. Teor. Fiz. **74**, 1137 (1978), sov. Phys. JETP **47**, 597 (1978)].

[22] H. van Houten *et al.*, Europhys. Lett. **5**, 721 (1988).

[23] H. van Houten *et al.*, Phys. Rev. B **39**, 8556 (1989).

[24] M. L. Roukes *et al.*, Phys. Rev. Lett. **59**, 3011 (1987).

[25] C. W. J. Beenakker and H. van Houten, in *Electronic Properties of Multilayers and Low-Dimensional Semiconductor Structures*, edited by J. M. Chamberlain, L. Eaves, and J. C. Portal (Plenum Press, New York, 1990), p. 75.

[26] D. R. Hofstadter, Phys. Rev. B **14**, 2239 (1976).

[27] D. Weiss, K. v. Klitzing, K. Ploog, and G. Weimann, Europhys. Lett. **8**, 179 (1989).

[28] C. W. J. Beenakker, Phys. Rev. Lett. **62**, 2020 (1989).

[29] R. R. Gerhardts, D. Weiss, and K. v. Klitzing, Phys. Rev. Lett. **62**, 1173 (1989).

[30] K. Ensslin and P. M. Petroff, Phys. Rev. B **41**, 12307 (1990).

[31] M. L. Roukes and A. Scherer, Bull. Am. Phys. Soc. **34**, 633 (1989).

[32] D. Weiss *et al.*, Appl. Phys. Lett. **58**, 2960 (1991).

[33] Y. Aharonov and D. Bohm, Phys. Rev. **115**, 485 (1959).

[34] R. A. Webb, S. Washburn, C. P. Umbach, and R. B. Laibowitz, Phys. Rev. Lett. **54**, 2696 (1985).

[35] N. W. Ashcroft and N. D. Mermin, *Solid State Physics* (Holt, Rinehart and Winston, New York, 1976).

[36] P. A. Lee and D. S. Fisher, Phys. Rev. Lett. **47**, 882 (1981).

[37] G. Bergmann, Phys. Rev. B **28**, 2914 (1983).

[38] G. Bergmann, Phys. Rep. **107**, 1 (1984).

[39] D. Y. Sharvin and Y. V. Sharvin, Pis'ma Zh. Eksp. Teor. Fiz. **34**, 285 (1981), [JETP Lett. **34**, 272 (1981)].

[40] B. Pannetier, J. Chaussy, R. Rammal, and P. Gandit, Phys. Rev. Lett. **53**, 718 (1984).

[41] B. Pannetier, J. Chaussy, R. Rammal, and P. Gandit, Phys. Rev. B **31**, 3209 (1985).

[42] G. J. Dolan, J. C. Licini, and D. J. Bishop, Phys. Rev. Lett. **56**, 1493 (1986).

[43] B. L. Altshuler *et al.*, Pis'ma Zh. Eksp. Teor. Fiz. **35**, 476 (1982), [JETP Lett. **35**, 588 (1982)].

[44] F. R. Ladan and J. Maurer, C. R. Acad. Sci. (Paris) Ser. II **297**, 227 (1983).

[45] M. Gijs, C. V. Haesendonck, and Y. Bruynseraede, Phys. Rev. Lett. **52**, 2069 (1984).

[46] C. Cavalloni and W. Joss, Phys. Rev. B **35**, 7338 (1987).

[47] D. J. Bishop, J. C. Licini, and G. J. Dolan, Appl. Phys. Lett. **46**, 1000 (1985).

[48] G. K. White, *Experimental Techniques in Low-Temperature Physics 3e* (Oxford University Press, Oxford, 1968).

[49] R. C. Richardson and E. N. Smith, *Experimental Techniques in Condenced Matter Physics at Low Temperatures* (Addison-Wesley, New York, 1988).

[50] H. Sakaki, Jpn. J. Appl. Phys. **19**, L735 (1980).

[51] K. Nakamura *et al.*, Appl. Phys. Lett. **56**, 385 (1990).

[52] J. Melngailis, J. Vac. Sci. Technol. B **5**, 469 (1987).

[53] J. Spector *et al.*, Surf. Sci. **228**, 283 (1990).

[54] F. Nihey *et al.*, Appl. Phys. Lett. **57**, 1218 (1990).

[55] K. K. Choi, D. C. Tsui, and S. C. Palmateer, Phys. Rev. B **32**, 5540 (1985).

[56] M. Büttiker, Phys. Rev. B **38**, 9375 (1988).

[57] L. W. Molenkamp *et al.*, Phys. Rev. B **41**, 1274 (1990).

[58] K. Tsukagoshi *et al.*, Appl. Phys. Lett. **62**, 1609 (1993).

[59] H. van Houten, C. W. J. Beenakker, B. J. van Wees, and J. E. Mooij, Surf. Sci. **196**, 144 (1988).

[60] S. D. Sarma and F. Stern, Phys. Rev. B **32**, 8442 (1985).

[61] J. Spector *et al.*, Appl. Phys. Lett. **56**, 967 (1990).

[62] D. Weiss *et al.*, Phys. Rev. Lett. **66**, 2790 (1991).

[63] R. Fleischmann, T. Geisel, and R. Ketzmerick, Phys. Rev. Lett. **68**, 1367 (1992).

[64] R. Kubo, J. Phys. Soc. Jpn. **12**, 570 (1957).

[65] E. M. Baskin *et al.*, Pis'ma Zh. Eksp. Teor. Fiz. **55**, 649 (1992), [JETP Lett. **55**, 678 (1992)].

[66] J. Takahara *et al.*, Jpn. J. Appl. Phys. **31**, 3786 (1992).

[67] J. Machta and R. Zwanzig, Phys. Rev. Lett. **50**, 1959 (1983).

[68] G. Timp *et al.*, Phys. Rev. Lett. **58**, 2814 (1987).

[69] C. J. B. Ford *et al.*, J. Phys. C **21**, L325 (1988).

[70] P. H. M. van Loosdrecht *et al.*, Phys. Rev. B **38**, 10162 (1988).

[71] B. J. van Wees *et al.*, Phys. Rev. Lett. **62**, 2523 (1989).

[72] F. Nihey and K. Nakamura, Physica B **184**, 398 (1993).

[73] M. Büttiker, Y. Imry, and R. Landauer, Phys. Lett. **96A**, 365 (1983).

[74] C. P. Umbach *et al.*, Phys. Rev. Lett. **56**, 386 (1986).

[75] G. M. Gusev *et al.*, Pis'ma Zh. Eksp. Teor. Fiz. **55**, 129 (1992), [JETP lett. **55**, 123 (1992)].

[76] B. L. Altshuler, A. G. Aronov, and B. Z. Spivak, Pis'ma Zh. Eksp. Teor. Fiz. **33**, 101 (1981), [JETP Lett. **33**, 94 (1981)].

[77] K. Tsubaki, T. Honda, and Y. Tokura, Surf. Sci. **263**, 392 (1992).

[78] F. Nihey, S. W. Hwang, and K. Nakamura, Phys. Rev. B **51**, 4649 (1995).

[79] B. Doucot and R. Rammal, Phys. Rev. Lett. **55**, 1148 (1985).

[80] B. Doucot and R. Rammal, J. Phys. (Paris) **47**, 973 (1986).

[81] H. W. Jiang, C. E. Johnson, and K. L. Wang, Phys. Rev. B **46**, 12830 (1992).

[82] T. Wang *et al.*, Phys. Rev. Lett. **72**, 709 (1994).

[83] R. J. F. Hughes *et al.*, J. Phys.: Condens. Matter **6**, 4763 (1994).

[84] S. V. Kravchenko, W. Mason, J. E. Furneaux, and V. M. Pudalov, Phys. Rev. Lett. **75**, 910 (1995).

[85] M. P. A. Fisher, Phys. Rev. Lett. **65**, 923 (1990).

[86] A. F. Hebard and M. A. Paalanen, Phys. Rev. Lett. **65**, 927 (1990).

[87] H. W. Jiang, C. E. Johnson, K. L. Wang, and S. T. Hannahs, Phys. Rev. Lett. **71**, 1439 (1993).

[88] N. F. Mott and G. A. Davis, *Electronic Process in Non-crystalline Materials* (Clarendon, Oxford, 1979).

[89] A. L. Efros and B. I. Shklovskii, J. Phys. C **8**, L49 (1975).

[90] A. L. Efros, J. Phys. C **9**, 2021 (1976).

[91] B. I. Shklovskii and A. L. Efros, *Electronic Properties of Doped Semiconductors* (Springer, Berlin, 1984).

[92] A. M. M. Pruisken, in *The Quantum Hall Effect, 2nd ed.*, edited by R. E. Prange and S. M. Girvin (Springer, Berlin, 1990), p. 117.

[93] B. Huckestein, Rev. Mod. Phys. **67**, 357 (1995).

[94] R. Rammal, J. Phys. (Paris) **46**, 1345 (1985).